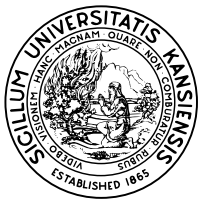

Aeroelastic Calculations of a Business Jet Configuration Using the USTSD Code

Thomas M. Hermann
University of Kansas

July 31, 2001

Abstract

This report documents the evaluation of the aeroelastic analysis capability of the Unsteady Transonic Small-Disturbance code (USTSD) applied to a business jet configuration. In USTSD, the solution to the transonic small-disturbance equation is calculated in the frequency domain. Pressure distributions, lift, drag and pitching moment coefficients are calculated and compared with available data. With a 2D boundary layer analysis included, the finite-difference solution of the non-conservative TSD equation tends to provide better correlation with data as compared with the conservative formulation in steady flow. In flutter analysis, the non-conservative formulation generates a higher flutter speed than the conservative formulation.

Contents

List of Figures

List of Tables

Nomenclature

Symbol	Definition
a	Speed of sound
a_∞	Freestream speed of sound
a_{nj}	In-phase force amplitude
b_{nj}	Out-of-phase force amplitude
b_o	Characteristic length (7.263 ft)
C_f	Flutter speed index
C_p	Pressure coefficient
c_r	Root chord length (11.62 ft)
c_t	Root tip length (3.04 ft)
F	Instantaneous wing surface vertical location
f	Vertical elastic deformation motion
f^s	Wing surface shape
f^v	Structural displacement
g	Artificial damping
i	Unit vector in the x-direction; or
	Imaginary unit
j	Unit vector in the y-direction
k	Unit vector in the z-direction; or
	Reduced frequency
K	Generalized stiffness
m	Model mass
M	Generalized mass
M_∞	Freestream Mach number

Symbol	Definition
$\bar{p}$	Lifting pressure amplitude
q_n	Generalized coordinate of the n^{th} mode
$\bar{q}_n$	Generalized coordinate amplitude of the n^{th} mode
q_∞	Freestream dynamic pressure
Q_n	Generalized force of the n^{th} mode
$\bar{Q}_n$	Generalized force amplitude of the n^{th} mode
s	Wing semi-span
T	Kinetic energy
U	Potential Energy; or
	Velocity in the x-direction
V	Velocity in the y-direction; or
	Frustrum volume
V_f	Flutter speed
V_∞	Freestream velocity
W	Velocity in the z-direction
x, y, z	Global coordinates
X, Y, Z	Local coordinates
Z	Wing reference plane location
z_n	Modal deflection of the n^{th} mode

Greek	
μ	Mass ratio
ω_o	Reference frequency (17.38 Hz)
ρ	Density
δ	Phase angle between the motion and response, or
	Dirac's delta function
λ	Eigenvalue
Φ	Total velocity potential
ϕ	Small-disturbance velocity potential
γ	Ratio of specific heats
ω	Frequency
α^*	Instantaneous pitch angle
$\bar{\alpha}$	Pitch magnitude
Γ	Circulation

Subscript	Definition
t	Differentiation with respect to time
x	Differentiation in the x-direction
y	Differentiation in the y-direction
z	Differentiation in the z-direction

Superscript	Definition
(i)	In-phase
(o)	Out-of-phase
s	Steady
u	Unsteady

Acronym	Definition
CAP-TSD	Computational Aeroelasticity Program - Transonic-Small Disturbance
CFL3D	Computational Fluids Laboratory 3-Dimensional
ENS3DAE	Euler/Navier-Stokes Three-Dimensional AeroElastic
TSD	Transonic-Small Disturbance
USTSD	Unsteady Transonic-Small Disturbance

Chapter 1

Introduction

This report documents the evaluation of the aeroelastic analysis capability of the Unsteady Transonic Small-Disturbance code (USTSD). USTSD is capable of calculating the steady and unsteady aerodynamic characteristics of general aircraft configurations. In this report, the USTSD is used to calculate the generalized aerodynamic forcing function required for the solution of the flutter equation.

Current computational aeroelastic methods are presented in Reference [2]. In this reference, the time domain methods CAP-TSD, CFL3D and ENS3DAE are presented. Transonic small-disturbance theory (TSD) is utilized in CAP-TSD. Both CFL3D and ENS3DAE calculate solutions of the Euler and Navier-Stokes equations. The aerodynamic geometry and structural dynamics of the model are required to perform aeroelastic analysis with these codes. Orthogonal modes of vibration are used to represent the structural dynamics. The mode shapes are interpolated from the modal grid to the computational grid on which the aerodynamic solution is obtained. For the Euler and Navier-Stokes solutions, the grid must move with the surface. The TSD boundary conditions are applied on a mean plane and therefore the moving grid is not required. Once the time-domain solution is obtained, it must be processed to generate the generalized aerodynamic forcing function for the flutter equation. Finally, the stability of the system is calculated.

Experience from previous computational aeroelastic flutter analysis in the time-domain suggests that approximately 100 analysis cycles are required to determine the flutter boundary for a range of Mach numbers and dynamic pressures. The associated computational cost limits the suitability of these methods to analysis of conditions considered critical based on linear solutions.

This cost is not acceptable for multi-disciplinary design problems that require as many as 10^5 to 10^6 evaluations of the system (Ref. [2]).

One approach to reducing the computational cost is to perform the analysis in the frequency domain. By performing the analysis in the frequency domain, the post-processing of the results to obtain the generalized aerodynamic forcing coefficient is negated. Furthermore, when the TSD equation is solved in the frequency domain, the unsteady equations are similar in form to the steady equation and can be solved using the same solution algorithm. Thus, significant computational savings can be realized by performing the solution in the frequency domain.

In the USTSD code, the frequency domain approach is applied to the TSD equation. The frequency domain TSD equation is formulated from the time-domain equation using the method of harmonic averaging (Ref. [6, 11]). The USTSD code has been developed at the University of Kansas over the past ten years for jet fighter configurations. Since fighter wings are thin (less than 6% in thickness ratio), it is not certain how the USTSD code will perform for the aeroelastic analysis of a business jet configuration that has a thicker wing. The capability of the code to perform aeroelastic analysis of a business jet configuration is presented in this report.

Chapter 2

Unsteady Transonic Small-Disturbance Theory

Formulation of the unsteady transonic small-disturbance (TSD) equation used in the USTSD is presented in this chapter. In the time domain, the unsteady TSD equation is derived from the full potential equation. Using the method of harmonic averaging, the unsteady TSD equation is then expressed in the frequency domain. The chapter is concluded with the formulation of the boundary conditions.

2.1 Time Domain

The unsteady TSD equation is derived from the full potential equation. The full potential equation is a simplification of the Euler equations assuming isentropic and irrotational flow. In transonic flow, the assumption of isentropic flow is not valid. Despite this inconsistency in the formulation of the potential equation, adequate transonic flow estimations have been performed using the full potential equation (Ref. [16]). The full potential equation is expressed:

$$\begin{aligned} &\Phi_{tt} + 2U\Phi_{tx} + 2V\Phi_{ty} + 2W\Phi_{tz} \\ &\quad = \left(a^2 - U^2\right)\Phi_{xx} + \left(a^2 - V^2\right)\Phi_{yy} + \left(a^2 - W^2\right)\Phi_{zz} \\ &\quad - 2UV\Phi_{xy} - 2UW\Phi_{xz} - 2VW\Phi_{yz} \end{aligned} \tag{2.1}$$

where Φ is the velocity potential, U is the velocity in the X direction, V

is the velocity in the Y direction, W is the velocity in the Z direction, a is the local speed of sound and t is time. Subscripts denote partial differentiation of the variable with respect to the subscript variable. The unsteady TSD equation is a simplification of the full potential equation. The velocity potential is assumed to be the sum of the freestream potential and a perturbation or small-disturbance velocity potential, $\phi(x, y, z, t)$:

$$\Phi(x, y, z, t) = V_\infty x + \phi(x, y, z, t) \tag{2.2}$$

The first step of deriving the unsteady TSD equation from Equation 2.1 is to express the local velocities and speed of sound as gradient components of the velocity potential. After substituting the expressions for velocity and speed of sound into the full potential equation, small-disturbance assumptions are applied and higher order terms are subtracted from the equation, except the ϕ_x term in the coefficient of ϕ_{xx}, since it is not small compared with the other terms in the coefficient. Finally, velocity and speed of sound terms are recast using Mach number, resulting in the classical unsteady TSD equation:

$$\frac{\phi_{tt}}{a_\infty^2} + 2\frac{M_\infty^2 \phi_{tx}}{V_\infty} = \left[\left(1 - M_\infty^2\right) - (\gamma + 1)\frac{M_\infty^2 \phi_x}{V_\infty}\right]\phi_{xx} + \phi_{yy} + \phi_{zz} \tag{2.3}$$

Two corrections are applied to Equation 2.3 to improve the correlation with experiment. For improved calculation of swept-back wings, the nonlinear terms $2M_\infty^2 \phi_y \phi_{xy}/V_\infty$ and $(\gamma - 1)\, M_\infty^2 \phi_x \phi_{yy}/V_\infty$ are included (Ref. [13]). As shown by Krupp [10], prediction of the shock jump condition is improved by setting the exponent of the Mach number to 1.75 when it is a coefficient of $\phi_x \phi_{xx}$. The corrected unsteady TSD equation is expressed:

$$\begin{aligned} &\frac{\phi_{tt}}{a_\infty^2} + 2\frac{M_\infty^2 \phi_{tx}}{V_\infty} \\ &= \left[\left(1 - M_\infty^2\right) - (\gamma + 1)\frac{M_\infty^{1.75} \phi_x}{V_\infty}\right]\phi_{xx} - 2\frac{M_\infty^2 \phi_y \phi_{xy}}{V_\infty} \\ &+ \left[1 - (\gamma - 1)\frac{M_\infty^2 \phi_x}{V_\infty}\right]\phi_{yy} + \phi_{zz} \end{aligned} \tag{2.4}$$

Recast in conservative form:

$$\begin{aligned}
&\frac{\partial}{\partial t}\left(\frac{1}{a_\infty^2}\phi_t + 2\frac{M_\infty^2}{V_\infty}\phi_x\right) \\
&= \frac{\partial}{\partial x}\left[\left(1-M_\infty^2\right)\phi_x - \frac{(\gamma+1)\,M_\infty^{1.75}}{2V_\infty}\phi_x^2 + \frac{(\gamma-3)\,M_\infty^2}{V_\infty}\phi_y^2\right] \\
&+ \frac{\partial}{\partial y}\left[\phi_y - \frac{(\gamma-1)\,M_\infty^2}{V_\infty}\phi_x\phi_y\right] + \frac{\partial}{\partial z}\left(\phi_z\right)
\end{aligned} \tag{2.5}$$

2.2 Frequency Domain

The unsteady TSD equation is solved in the frequency domain in the USTSD program. Solutions of the unsteady TSD equation in the time domain are generally accomplished using an implicit solution algorithm. Formulation of the equation in the frequency domain is accomplished using the theory of harmonic averaging [14]. Successful application of the theory of harmonic averaging to transonic aerodynamic problems has been shown in References [7, 8, 9, 17]. The advantage of this formulation is that a steady flow solution algorithm can be utilized, reducing the computational requirements.

To apply the method of harmonic averaging, the small-disturbance velocity potential is expressed as the superposition of steady and unsteady components:

$$\phi\left(X,Y,Z,t\right) = \phi^s\left(X,Y,Z\right) + \phi^u\left(X,Y,Z\right)\cos\left(\theta+\delta\right) \tag{2.6}$$

Where ϕ^s is the steady component and ϕ^u is the unsteady component. Theta is defined as $\theta = \omega t$. The phase angle is δ. For notational purposes, in-phase and out-of-phase velocity potentials are also defined:

$$\begin{aligned}
\phi^i &= \phi^s + \phi^{u(i)} \\
\phi^o &= \phi^s + \phi^{u(o)}
\end{aligned}$$

where:

$$\begin{aligned}
\phi^{u(i)} &= \phi^u\cos\delta \\
\phi^{u(o)} &= \phi^u\sin\delta
\end{aligned}$$

The frequency domain TSD equation is obtained by substituting the new velocity potential definition, Equation 2.6, into Equation 2.4. The theory of harmonic averaging is applied to the resulting equation to remove the time-dependent terms. This results in modeling the problem as an in-phase and out-of-phase solutions superposed on a steady state solution. The steady state TSD equation is obtained by neglecting all unsteady terms from the frequency domain TSD equation. The steady state TSD equation is expressed:

$$\begin{aligned} & \frac{\partial}{\partial x}\left[\left(1-M_\infty^2\right)\phi_x^s-(\gamma-1)\frac{M_\infty^{1.75}}{2V_\infty}(\phi_x^s)^2+(\gamma-3)\frac{M_\infty^2}{V_\infty}\left(\phi_y^s\right)^2\right] \\ + & \frac{\partial}{\partial y}\left[\phi_y^s-(\gamma-1)\frac{M_\infty^2}{V_\infty}\phi_x^s\phi_y^s\right]+\frac{\partial}{\partial z}\left(\phi_z^s\right)=0 \end{aligned} \tag{2.7}$$

Three forms of averaging are performed to obtain the equation for the unsteady response. First, the steady terms are subtracted from the frequency domain TSD equation, integrating the result over one cycle to obtain an overall average unsteady response:

$$-\frac{(\gamma-1)M_\infty^{1.75}}{V_\infty}\phi_x^u\phi_{xx}^u-\frac{2M_\infty^2}{V_\infty}\phi_y^u\phi_{xy}^u+\frac{(\gamma-1)M_\infty^2}{V_\infty}\phi_x^u\phi_{yy}^u=0 \tag{2.8}$$

Then the in-phase average response is formulated by multiplying the frequency domain TSD by $\cos\theta$ and integrating over one cycle:

$$\begin{aligned} & -\frac{\omega^2}{a_\infty^2}\phi^{u(i)}-2\frac{\omega M_\infty^2}{V_\infty}\phi_x^{u(o)} \\ = & \frac{\partial}{\partial x}\left[\left(1-M_\infty^2\right)\left(\phi_x^i\right)-(\gamma-1)\frac{M_\infty^{1.75}}{2V_\infty}\left(\phi_x^i\right)^2+(\gamma-3)\frac{M_\infty^2}{V_\infty}\left(\phi_y^i\right)^2\right] \\ + & \frac{\partial}{\partial y}\left[\phi_y^i-(\gamma-1)\frac{M_\infty^2}{V_\infty}\phi_x^i\phi_y^i\right]+\frac{\partial}{\partial z}\left(\phi_z^i\right) \end{aligned} \tag{2.9}$$

Finally, the out-of-phase average response is formulated by multiplying frequency domain TSD by $\sin\theta$ and integrating over one cycle:

$$
\begin{aligned}
&-\frac{\omega^2}{a_\infty^2}\phi^{u(o)} - 2\frac{\omega M_\infty^2}{V_\infty}\phi_x^{u(i)} \\
&= \frac{\partial}{\partial x}\left[\left(1-M_\infty^2\right)\left(\phi_x^o\right) - \left(\gamma-1\right)\frac{M_\infty^{1.75}}{2V_\infty}\left(\phi_x^o\right)^2 + \left(\gamma-3\right)\frac{M_\infty^2}{V_\infty}\left(\phi_y^o\right)^2\right] \\
&+ \frac{\partial}{\partial y}\left[\phi_y^o - \left(\gamma-1\right)\frac{M_\infty^2}{V_\infty}\phi_x^o\phi_y^o\right] + \frac{\partial}{\partial z}\left(\phi_z^o\right) \qquad (2.10)
\end{aligned}
$$

To obtain the in-phase unsteady response, the overall average response (Eqn 2.8) is multiplied by $\cos^2\delta$ and added to the steady flow response (Eqn 2.7) and the in-phase average response (Eqn 2.9). The final in-phase frequency domain unsteady TSD equation can now be expressed:

$$
\begin{aligned}
&-\frac{\omega^2}{a_\infty^2}\phi^{u(i)} - 2\frac{\omega M_\infty^2}{V_\infty}\phi_x^{u(o)} \\
&= \frac{\partial}{\partial x}\left[\left(1-M_\infty^2\right)\left(\phi_x^i\right) - \left(\gamma-1\right)\frac{M_\infty^{1.75}}{2V_\infty}\left(\phi_x^i\right)^2 + \left(\gamma-3\right)\frac{M_\infty^2}{V_\infty}\left(\phi_y^i\right)^2\right] \\
&+ \frac{\partial}{\partial y}\left[\phi_y^i - \left(\gamma-1\right)\frac{M_\infty^2}{V_\infty}\phi_x^i\phi_y^i\right] + \frac{\partial}{\partial z}\left(\phi_z^i\right) \qquad (2.11)
\end{aligned}
$$

Similarly, to obtain the out-of-phase unsteady response, the overall average response (Eqn 2.8) is multiplied by $\sin^2\delta$ and added to the steady flow response (Eqn 2.7) and the out-of-phase average response (Eqn 2.10). The final out-of-phase frequency domain unsteady TSD equation can now be expressed:

$$
\begin{aligned}
&\frac{\omega^2}{a_\infty^2}\phi^{u(o)} - 2\frac{\omega M_\infty^2}{V_\infty}\phi_x^{u(i)} \\
&= \frac{\partial}{\partial x}\left[\left(1-M_\infty^2\right)\left(\phi_x^o\right) - \left(\gamma-1\right)\frac{M_\infty^{1.75}}{2V_\infty}\left(\phi_x^o\right)^2 + \left(\gamma-3\right)\frac{M_\infty^2}{V_\infty}\left(\phi_y^o\right)^2\right] \\
&+ \frac{\partial}{\partial y}\left[\phi_y^o - \left(\gamma-1\right)\frac{M_\infty^2}{V_\infty}\phi_x^o\phi_y^o\right] + \frac{\partial}{\partial z}\left(\phi_z^o\right) \qquad (2.12)
\end{aligned}
$$

Note that Equations 2.11 and 2.12 have the same form as the steady flow equation (Equation 2.7) if the unsteady terms on the left hand side are set to zero. In this form, the in-phase and out-of phase equations can be solved using the same solution algorithm as the steady flow equation.

2.3 Boundary Conditions

To solve the TSD equation, boundary conditions must be specified on the wing, body, wake and far-field. The wing and body boundary conditions are formulated to restrict flow from passing through the surface. Wake boundary conditions are formulated so that there are discontinuities in pressure across the wake. Far-field boundary conditions are broken into subsonic and supersonic conditions. For subsonic freestream flow, the boundary conditions are formulated so that there is zero flux normal to the boundary. In the case of supersonic freestream flow, far-field boundary conditions must be applied so that outgoing waves are not reflected. Formulation of the boundary conditions is presented in this section.

2.3.1 Wing Boundary Conditions

Wing boundary conditions are enforced on the wing reference plane. The wing reference plane approximates the wing with a planar sheet of zero thickness upon which the surface slopes are specified. For steady state calculations, the fluid velocity normal to the wing is zero. When considering unsteady flow, the fluid velocity normal to the wing is set equal to the velocity of the wing surface. Fixing the coordinate system with the flow field, the flow tangency condition is expressed:

$$\frac{\boldsymbol{D}F}{\boldsymbol{D}t} = \frac{\partial F}{\partial t} + \vec{V} \cdot \boldsymbol{\nabla} F = 0 \tag{2.13}$$

Velocities in Equation 2.13 must be expressed in terms of the small-disturbance potential. The velocity potential applied to the wing boundary condition in the fixed coordinate system is expressed:

$$\Phi = XV_\infty \cos\alpha + ZV_\infty \sin\alpha + \phi(X,Y,Z,t) \cong XV_\infty + ZV_\infty\alpha + \phi \tag{2.14}$$

The vector F is the instantaneous vertical location of the wing surface, defined by $F = Z - f(X,Y,t)$. The wing reference plane is vertically located at Z. To model the flutter motion, the function $f(X,Y,t)$ should express the vertical elastic deformation motion. However, the rigid pitching motion will also be included for pitch damping calculations. The motion is defined

in a moving coordinate system, illustrated in Figure 2.1. The equation is expressed as (Ref. [9]):

$$f(X,Y,t) = -f^v(x,y)\cos\theta + f^s(x,y)\cos\alpha^* - (x - x_p)\sin\alpha^* \tag{2.15}$$

where the relation between the fixed and moving coordinate system is:

$$X = (x - x_p)\cos\alpha^* + f^s(x,y)\sin\alpha^* + x_p \tag{2.16}$$

The function $f^v(x,y)$ describes the displacement of a structural mode shape in free oscillation. The function $f^s(x,y)$ describes the wing surface shape. The instantaneous pitch angle is $\alpha^*(t) = \bar{\alpha}\cos\theta$, where $\bar{\alpha}$ is the pitch amplitude.

The boundary condition is formulated by substituting Equation 2.14 for velocities and Equation 2.15 for the vector F into Equation 2.13. To maintain compatibility with the Krupp correction applied to the TSD equation, a Krupp-type [10] scaling factor, $1/M^{0.25}$, is applied to the boundary conditions. The wing boundary condition is expressed as:

$$\begin{aligned} \phi_z &= \frac{\omega\sin\theta}{M^{0.25}}\left[f^v\left(1+\bar{\alpha}^2\right) + \bar{\alpha}\,(x - x_p)\right] \\ &+ \frac{V_\infty}{M^{0.25}}\left(\frac{-f_x^v\cos\theta + f_x^s - \bar{\alpha}\cos\theta}{1 + \bar{\alpha} f_x^s\cos\theta} - \alpha\right) \end{aligned} \tag{2.17}$$

Now the method of harmonic averaging is applied to remove the time-dependent terms. This results in steady state, in-phase and out-of-phase equations. To apply the method of harmonic averaging, the normal velocity potential is redefined $\phi_z = \phi_z^s + \phi_z^u\cos(\theta + \delta)$. The steady state equation is formulated by neglecting all time dependent terms. It is expressed:

$$\phi^s = \frac{V_\infty}{M^{0.25}}\left(f_x^s - \alpha\right) \tag{2.18}$$

The in-phase response is formulated in 2 steps. First, the wing boundary equation is multiplied by $\cos\theta$, integrating the result over one cycle to obtain an in-phase average response. Then the average response is added to the steady state equation, Equation 2.18. The in-phase wing boundary condition becomes:

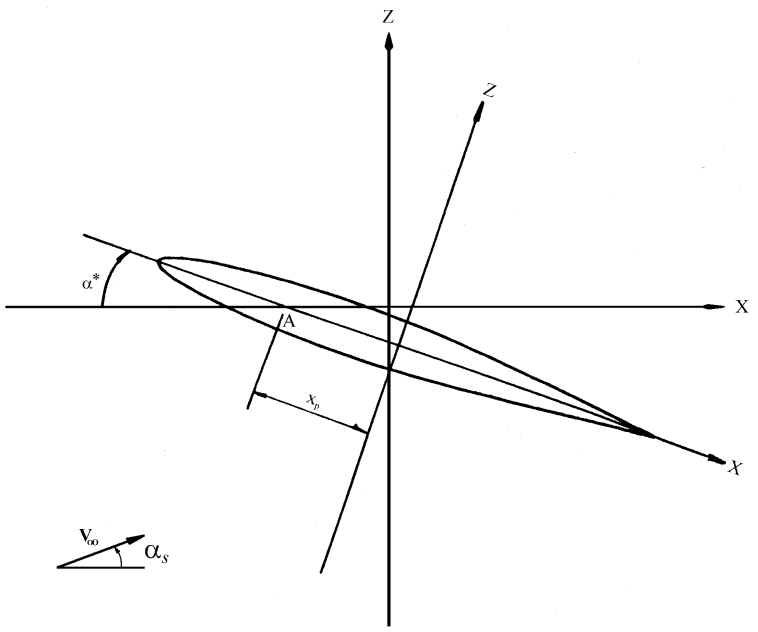

Figure 2.1: Relation between moving and fixed coordinate system.

$$\phi_z^i = \frac{V_\infty}{M^{0.25}} \left[f_x^s \left(1 - \alpha\bar{\alpha}\right) - f_x^v - \bar{\alpha} - \alpha \right] - \bar{\alpha} f_x^s \phi_z^s \tag{2.19}$$

The out-of-phase response is similarly formulated. First, the wing boundary equation is multiplied by $\sin\theta$, integrating the result over one cycle to obtain an out-of-phase average response. Then the average response is added to the steady state equation, Equation 2.18. The out-of-phase wing boundary condition becomes:

$$\phi_z^o = \frac{V_\infty}{M^{0.25}} \left(f_x^s - \alpha\right) - \frac{\omega}{M^{0.25}} \left[f^v \left(1 + \frac{\bar{\alpha} f_x^s}{4}\right) + \bar{\alpha}(x - x_p) \right] \tag{2.20}$$

2.3.2 Body Boundary Conditions

Body boundary conditions are enforced on a fixed length, constant cross-section rectangle denoted the boundary condition support surface (BCSS).

Use of the BCSS simplifies grid generation while applying the boundary conditions in a manner that is consistent with the accuracy of the unsteady TSD equations. On the upper and lower surfaces of the BCSS, the boundary condition is similar to Equation 2.19.

The upper and lower unsteady boundary conditions are based on the concept in slender body theory in which a distribution of doublets that perturb the flow to correspond to the shape of the body are specified on the body axis. The strength of the doublet distribution is proportional to the body cross-sectional area. This concept is applied to Equation 2.19 by multiplying the angle of attack terms by the cross section area, S_a. The in-phase component becomes:

$$\phi_z^i = \left(\frac{\partial z}{\partial x}\right)_b - S_a \left[\alpha + \bar{\alpha} + f_x^v\right] \tag{2.21}$$

The wing surface slope, f^s, has been replaced in Equation 2.21 by the body slope, $\partial z/\partial x$. Since the boundary condition is applied on a surface with finite radii in the TSD theory instead of on the axis, the doublet strength should be inversely proportional to the surface area. The surface area is proportional to the radius for a unit distance in the length-wise direction of the body. The adjusted upper and lower surface in-phase body boundary condition is expressed:

$$\phi_z^i = \left(\frac{\partial z}{\partial x}\right)_b - \sqrt{S_a} \left[\alpha + \bar{\alpha} + f_x^v\right] \tag{2.22}$$

Similarly, the out-of-phase body boundary condition is expressed:

$$\phi_z^o = \left(\frac{\partial z}{\partial x}\right)_b - \sqrt{S_a} \left(\alpha + \omega \left[f^v + \bar{\alpha}(x - x_p)\right]\right) \tag{2.23}$$

The boundary condition on the sides of the BCSS is simply expressed:

$$\phi_y = F_y \tag{2.24}$$

2.3.3 Wake Boundary Conditions

The wake boundary condition is defined such that the pressure difference across the wake vortex sheet is zero. This is equivalent to satisfying the circulation convection equation:

$$\frac{\boldsymbol{D}\Gamma}{\boldsymbol{D}t} = \frac{\partial\Gamma}{\partial t} + \langle U\rangle\frac{\partial\Gamma}{\partial x} = 0 \tag{2.25}$$

where $\langle U\rangle$ is the local average velocity, defined as the average of velocity components U above and below the wake. Circulation at the trailing edge can be obtained numerically by calculating the difference of velocity potentials above and below the wake. The circulation is defined as:

$$\Gamma^u = \nabla\phi^u \cos(\theta + \delta) \tag{2.26}$$

where $\nabla\phi^u = \phi^{u^+} - \phi^{u^-}$. The superscripts "+" and "-" denote limits as the sheet is approached from above and below, respectively. Expressing $\langle U\rangle$ in term of the unsteady velocity potential results in:

$$\langle U^u\rangle = \langle 1 + \phi^s_x + \phi^u_x \cos(\theta + \delta)\rangle \tag{2.27}$$

Then, using the averaging technique, the in-phase and out-of-phase components for the wake boundary conditions are obtained:

$$\begin{aligned} -\left(\frac{\omega}{V_\infty}\right)\Gamma^{u(o)} + \langle U^{u(i)}\rangle\Gamma^{u(i)} &= 0 \\ \left(\frac{\omega}{V_\infty}\right)\Gamma^{u(i)} + \langle U^{u(o)}\rangle\Gamma^{u(o)} &= 0 \end{aligned} \tag{2.28}$$

where $\langle U^{u(i)}\rangle = \langle 1 + \phi^{u(i)}_x\rangle$ and $\langle U^{u(o)}\rangle = \langle 1 + \phi^{u(o)}_x\rangle$

2.4 Far-Field Boundary Conditions

Far-field boundary conditions are prescribed on the side and outflow boundary of the computational domain. The outflow boundary is defined as the

boundary downstream of the model in the x-direction. Side boundaries bound the model above and below in the z-direction and on the left and right in the y-direction. The conditions are formulated separately for subsonic and supersonic freestream flow. For subsonic freestream flow, the boundary conditions are specified such that there is no perturbation velocity component normal to the boundary. On the boundaries normal to the z-axis above and below the model, the boundary conditions are:

$$\begin{aligned} \phi_z^s &= 0 \\ \phi_z^i &= 0 \\ \phi_z^o &= 0 \end{aligned} \tag{2.29}$$

The boundary conditions on the left and right of the model in the y-direction are:

$$\begin{aligned} \phi_y^s &= 0 \\ \phi_y^i &= 0 \\ \phi_y^o &= 0 \end{aligned} \tag{2.30}$$

And on the outflow boundary:

$$\begin{aligned} \phi_x^s &= 0 \\ \phi_x^i &= 0 \\ \phi_x^o &= 0 \end{aligned} \tag{2.31}$$

When the freestream flow is supersonic, the boundary conditions are formulated from Equation 2.3 using the method of characteristics so that disturbances are not reflected from the boundary. For notational purposes, define:

$$\begin{aligned} A &= M_\infty^2 \\ B &= 2M_\infty^2 \\ E &= 1 - M_\infty^2 \\ D^2 &= 8A + \frac{B^2}{E} \end{aligned}$$

In the far-field, linear small-disturbance assumptions are applied to Equation 2.3, to result in:

$$A\phi_{tt} + B\phi_{xt} = E\phi_{xx} + \phi_{yy} + \phi_{zz} \tag{2.32}$$

Although Equation 2.32 is a four-dimensional equation, the method of characteristics will be applied to only two of the dimensions at each boundary. Simplification to two-dimensions at the far-field boundary is consistent with linear small-disturbance assumptions and does not detract from the accuracy of the solution. Formulation of the steady boundary conditions from Equation 2.32 will be illustrated on the outflow boundary. On the outflow boundary, disturbances in the spanwise direction are ignored. Equation 2.32 is expressed in the characteristic coordinates by the transformation:

$$\begin{aligned} s &= \frac{1}{2}x - \frac{\sqrt{E}}{2}z \\ n &= \frac{1}{2}x + \frac{\sqrt{E}}{2}z \end{aligned} \tag{2.33}$$

In Equation 2.33, the direction s is parallel to the characteristics. The direction n is normal to the characteristics. Expressed in characteristic coordinates, Equation 2.32 is:

$$A\phi_{tt} + B\left(\frac{\phi_{st} + \phi sn}{2}\right) = E\phi_{ss} \tag{2.34}$$

Applying the linear small-disturbance theory, ϕ_{sn} is deducted from Equation 2.34. Utilizing another coordinate transformation, Equation 2.34 can be expressed as the two-dimensional wave equation. The coordinate transformation is:

$$\begin{aligned} \xi &= \frac{s}{\sqrt{E}} \\ \tau &= \frac{B}{ED}s + \frac{2}{D}t \end{aligned} \tag{2.35}$$

where:

$$D^2 = 8A + \frac{B^2}{E}$$

The resulting equation is:

$$\phi_{\tau\tau} = \phi_{\xi\xi} \tag{2.36}$$

Equation 2.36 and the Cauchy data form a system of three linear equations and three unknowns, $\phi_{\xi\xi}$, $\phi_{\xi\tau}$ and $\phi_{\tau\tau}$.

$$\begin{aligned} \phi_{\xi\xi} - \phi_{\tau\tau} &= 0 \\ \phi_{\xi\xi}\, d\xi + \phi_{\xi\tau}\, d\tau &= d(\phi_\xi) \\ \phi_{\xi\tau}\, d\xi + \phi_{\tau\tau}\, d\tau &= d(\phi_\tau) \end{aligned} \tag{2.37}$$

The characteristic condition is the condition under which the determinant of this system is equal to zero:

$$\begin{vmatrix} 1 & 0 & -1 \\ d\xi & d\tau & 0 \\ 0 & d\xi & d\tau \end{vmatrix} = (\, d\tau)^2 - (\, d\xi)^2 = 0 \Rightarrow \frac{d\xi}{d\tau} = +1 \tag{2.38}$$

Equation 2.38 defines the characteristic lines. The relation that holds along the characteristic lines is determined by applying Cramer's rule to solve for the right hand side of Equation 2.37.

$$\begin{vmatrix} 1 & 0 & 0 \\ d\xi & d\tau & d(\phi_\xi) \\ 0 & d\xi & d(\phi_\tau) \end{vmatrix} = d(\phi_\tau)\, d\tau - d(\phi_\xi)\, d\xi = 0 \tag{2.39}$$

Integrating Equation 2.39 results in:

$$\phi_\tau + \phi_\xi = c \tag{2.40}$$

Equation 2.40 is only valid along the characteristic lines. For correct formulation of the far-field conditions, the constant, c, in Equation 2.40 equals

zero. To utilize Equation 2.40 in the USTSD, it must be mapped to the xy space. From the $\xi\tau$ space, Equation 2.40 is mapped to the st space:

$$\frac{D}{2}\phi_t + \left(\sqrt{E}\,\phi_s - \frac{B}{2\sqrt{E}}\phi_t\right) = 0 \tag{2.41}$$

Then, from the st space, Equation 2.41 is mapped to the xy space:

$$\frac{1}{2}\left(D - \frac{B}{\sqrt{E}}\right)\phi_t + \left(\sqrt{E}\,\phi_x - \phi_z\right) = 0 \tag{2.42}$$

Equation 2.42 is the equation for the boundary condition at the outflow boundary below the z datum line. Supersonic boundary conditions on the remaining boundaries are formulated using the same method. The resulting equation for z above the datum at the outflow boundary is:

$$\frac{1}{2}\left(D - \frac{B}{\sqrt{E}}\right)\phi_t + \left(\sqrt{E}\,\phi_x + \phi_z\right) = 0 \tag{2.43}$$

For the top boundary in the z-direction:

$$\frac{1}{2}\left(D - \frac{B}{\sqrt{E}}\right)\phi_t + \left(\sqrt{E}\,\phi_x + \phi_z\right) = 0 \tag{2.44}$$

For the bottom boundary in the z-direction:

$$\frac{1}{2}\left(D - \frac{B}{\sqrt{E}}\right)\phi_t + \left(\sqrt{E}\,\phi_x - \phi_z\right) = 0 \tag{2.45}$$

For the right hand side boundary in the y-direction:

$$\frac{1}{2}\left(D - \frac{B}{\sqrt{E}}\right)\phi_t + \left(\sqrt{E}\,\phi_x + \phi_y\right) = 0 \tag{2.46}$$

For the left hand side boundary in the y-direction:

$$\frac{1}{2}\left(D-\frac{B}{\sqrt{E}}\right)\phi_t+\left(\sqrt{E}\,\phi_x-\phi_y\right)=0 \tag{2.47}$$

The equations for the unsteady boundary conditions are formulated similarly. The in-phase outflow boundary condition above the z datum:

$$\frac{1}{2}\left(D-\frac{B}{\sqrt{E}}\right)\left(\frac{\omega}{V_\infty}\right)\phi^{u(o)}+\sqrt{E}\phi_x^i+\phi_z^i=0 \tag{2.48}$$

Out-of-phase outflow boundary condition above the z datum:

$$\frac{1}{2}\left(D-\frac{B}{\sqrt{E}}\right)\left(\frac{\omega}{V_\infty}\right)\phi^{u(i)}+\sqrt{E}\phi_x^o+\phi_z^o=0 \tag{2.49}$$

In-phase outflow boundary condition below the z datum:

$$\frac{1}{2}\left(D-\frac{B}{\sqrt{E}}\right)\left(\frac{\omega}{V_\infty}\right)\phi^{u(o)}+\sqrt{E}\phi_x^i-\phi_z^i=0 \tag{2.50}$$

Out-of-phase outflow boundary condition below the z datum:

$$\frac{1}{2}\left(D-\frac{B}{\sqrt{E}}\right)\left(\frac{\omega}{V_\infty}\right)\phi^{u(i)}+\sqrt{E}\phi_x^o-\phi_z^o=0 \tag{2.51}$$

In-phase top boundary condition in the z-direction:

$$\frac{1}{2}\left(D-\frac{B}{\sqrt{E}}\right)\left(\frac{\omega}{V_\infty}\right)\phi^{u(o)}+\sqrt{E}\phi_x^i+\phi_z^i=0 \tag{2.52}$$

Out-of-phase top boundary condition in the z-direction:

$$\frac{1}{2}\left(D-\frac{B}{\sqrt{E}}\right)\left(\frac{\omega}{V_\infty}\right)\phi^{u(i)}+\sqrt{E}\phi_x^o+\phi_z^o=0 \tag{2.53}$$

In-phase bottom boundary condition in the z-direction:

$$\frac{1}{2}\left(D-\frac{B}{\sqrt{E}}\right)\left(\frac{\omega}{V_\infty}\right)\phi^{u(o)}+\sqrt{E}\phi_x^i i\phi_z^i=0 \tag{2.54}$$

Out-of-phase bottom boundary condition in the z-direction:

$$\frac{1}{2}\left(D-\frac{B}{\sqrt{E}}\right)\left(\frac{\omega}{V_\infty}\right)\phi^{u(i)}+\sqrt{E}\phi_x^o-\phi_z^o=0 \tag{2.55}$$

In-phase right boundary condition in the y-direction:

$$\frac{1}{2}\left(D-\frac{B}{\sqrt{E}}\right)\left(\frac{\omega}{V_\infty}\right)\phi^{u(o)}+\sqrt{E}\phi_x^i+\phi_y^i=0 \tag{2.56}$$

Out-of-phase right boundary condition in the y-direction:

$$\frac{1}{2}\left(D-\frac{B}{\sqrt{E}}\right)\left(\frac{\omega}{V_\infty}\right)\phi^{u(i)}+\sqrt{E}\phi_x^o+\phi_y^o=0 \tag{2.57}$$

In-phase left boundary condition in the y-direction:

$$\frac{1}{2}\left(D-\frac{B}{\sqrt{E}}\right)\left(\frac{\omega}{V_\infty}\right)\phi^{u(i)}+\sqrt{E}\phi_x^o-\phi_y^o=0 \tag{2.58}$$

Out-of-phase left boundary condition in the y-direction:

$$\frac{1}{2}\left(D-\frac{B}{\sqrt{E}}\right)\left(\frac{\omega}{V_\infty}\right)\phi^{u(i)}+\sqrt{E}\phi_x^o-\phi_y^o=0 \tag{2.59}$$

Chapter 3

Linear Flutter Equation

Formulation of the linear flutter equation is presented in this section. The linear flutter equation is derived from the non-conservative Lagrange equation. The derivation presented in this chapter is adapted from Reference [3]. An artificial damping term is added to the equation. Use of the artificial damping term is commonly referred to as the "k" or "V-g" method. The non-conservative Lagrange equation is expressed as:

$$\frac{d}{dt}\left(\frac{\partial\left(T-U\right)}{\partial\dot{q}_n}\right)-\frac{\partial\left(T-U\right)}{\partial q_n}=Q_n \tag{3.1}$$

where T is the kinetic energy, U is the potential energy and q_n is the generalized coordinate. The elastic deformation of the system is described in terms of the structural mode shape, z_n, and the generalized coordinates:

$$z(x,y,t)=\sum_{n=1}^{N} z_n(x,y)q_n(t) \tag{3.2}$$

Equation 3.2 is similar in form to an eigenfunction expansion for an arbitrary function $z(x,y,t)$. The kinetic energy of the system is expressed in terms of the velocity of the distributed mass of the system:

$$T=\frac{1}{2}\iint m(x,y)\dot{z}(x,y,t)^2\,dx\,dy \tag{3.3}$$

Expressing Equation 3.3 in terms of the generalized coordinates:

$$T = \frac{1}{2}\left[\sum_{i=1}^{N}\sum_{j=1}^{N}\dot{q}_i(t)\dot{q}_j(t)\iint m(x,y)z_i(x,y)z_j(x,y)\,dx\,dy\right] \tag{3.4}$$

Recognizing that normal modes are orthogonal, the generalized mass of the i^{th} structural mode satisfies:

$$M_{ij} = \iint m(x,y)z_i z_j\,dx\,dy = \begin{cases} 0 & i \neq j \\ M_i & i = j \end{cases} \tag{3.5}$$

Equation 3.4 can be simplified to:

$$T = \frac{1}{2}\sum_{i=1}^{N}\dot{q}_i^2 M_i \tag{3.6}$$

Similarly, the potential energy is expressed in terms of the spring forces of the system:

$$U = \frac{1}{2}\sum_{i=1}^{N}\sum_{j=1}^{N}q_i q_j K_{ij} \tag{3.7}$$

Utilizing the orthogonality relation and the definition of natural frequency of an undamped system, $\omega = \sqrt{k/m}$, the generalized stiffness, K_{ij}, can be related to the generalized mass, M_i by $K_i = \omega_i^2 M_i$. ω_i is the natural frequency of the i^{th} mode. The potential energy can now be expressed in terms of the generalized mass:

$$U = \frac{1}{2}\sum_{i=1}^{N}q_i^2 M_i \omega_i^2 \tag{3.8}$$

The Lagrange Equation, Equation 3.1, can now be expressed in terms of the generalized coordinates and mass. Substituting Equation 3.6 and Equation 3.8 into Equation 3.1 results in:

$$\ddot{q}_n M_n + q_n \omega_n^2 M_n = Q_n \quad n = 1, 2, 3, \ldots \tag{3.9}$$

The first term on the left-hand side of Equation 3.9 represents the inertial forces acting on the system. The second term represents the spring forces arising from structural stiffness acting on the system. The term on the right-hand side represents the external, i.e. aerodynamic, forces acting on the system. Assume that the motion of the system and the forces acting on the system are harmonic:

$$\begin{aligned} q_n &= \bar{q}_n e^{i\omega t} \\ Q_n &= \bar{Q}_n e^{i\omega t} \end{aligned} \tag{3.10}$$

Substituting Equation 3.10 into Equation 3.9 results in:

$$\bar{q}_n \left(\omega_n^2 - \omega^2\right) M_n = \bar{Q}_n \quad n = 1, 2, 3, \ldots \tag{3.11}$$

The generalized force amplitude $\bar{Q}_n$ can be expressed as a function of the lifting pressure amplitude, $\Delta\bar{p}$, and the modal deflection. The lifting pressure amplitude is expressed:

$$\Delta\bar{p} = \sum_{j=1}^{N} \Delta\bar{p}_j(x, y, \omega, M_\infty)\frac{\bar{q}_j}{b_o} \tag{3.12}$$

In Equation 3.12, b_o is the reference length and $\Delta\bar{p}_j$ is the normalized lifting pressure amplitude due to the motion of the jth structural mode. The lifting pressure amplitude is determined from the unsteady aerodynamic calculation in the frequency domain. Since the calculation is performed in the frequency domain, the lifting pressure amplitude for each mode is expressed as in-phase and out-of-phase components. The overall in-phase and out-of-phase pressure force amplitudes are calculated by integrating over the aircraft surface:

$$\begin{aligned} a_{nj} &= \iint \Delta\bar{C}^i_{pj} z_n(x, y)\, d\hat{x}\, d\hat{y} \\ b_{nj} &= \iint \Delta\bar{C}^o_{pj} z_n(x, y)\, d\hat{x}\, d\hat{y} \end{aligned} \tag{3.13}$$

In Equation 3.13, $\hat{x} = x/b_o$ and $\hat{y} = y/b_o$. The lifting pressure coefficient amplitudes are related to the lifting pressure amplitudes by:

$$\begin{aligned} \Delta\bar{C}^{i}_{pj} &= \frac{\Delta\bar{p}^{i}_{j}}{q_\infty} \\ \Delta\bar{C}^{o}_{pj} &= \frac{\Delta\bar{p}^{o}_{j}}{q_\infty} \end{aligned} \tag{3.14}$$

The i superscript refers to the in-phase components and the o superscript refers to the out-of-phase component. q_∞ is the freestream dynamic pressure. The generalized force amplitude is now expressed:

$$\begin{aligned} \bar{Q}_n &= \iint z_n(x,y)\Delta\bar{p}\,dx\,dy \\ &= q_\infty b_o^2 \sum_{j=1}^{N} \left[(a_{nj} + ib_{nj}) \frac{\bar{q}_j}{b_o} \right] \end{aligned} \tag{3.15}$$

Substituting Equation 3.15 into Equation 3.11 results in the flutter equation. To better approximate the actual system, an artificial structural damping term, g, is introduced. The resulting equation is expressed:

$$\bar{q}_n \left[\omega_n^2 (1 + ig) - \omega^2 \right] M_n = q_\infty b_o^2 \sum_{j=1}^{N} \left[(a_{nj} + ib_{nj}) \frac{\bar{q}_j}{b_o} \right] \tag{3.16}$$

Equation 3.16 is non-dimensionalized by collecting all terms on the left side and multiplied by:

$$\frac{1}{M_n} \left(\frac{\omega_o}{\omega_n} \right) \left(\frac{b_o^2}{b_o V_\infty^2} \right)$$

where ω_o is a reference frequency and V_∞ is the freestream velocity. The non-dimensionalized Equation 3.16 becomes:

$$\sum_{j=1}^{N} \left\{ \frac{\rho b_o^3 \omega_o^2}{2 M_n \omega_n^2} (a_{nj} + ib_{nj}) \frac{\bar{q}_j}{b_o} + \left[\left(\frac{\omega}{\omega_n} \right)^2 \frac{\omega_o {b_o}^2}{V_\infty} - \left(\frac{\omega_o b_o}{V_\infty} \right)^2 (1 + ig) \right] \frac{\bar{q}_n}{b_o} \right\} = 0 \tag{3.17}$$

The system of equations formed by Equation 3.17 is more clearly expressed by defining:

$$\begin{aligned}
\delta_{nj} &= \begin{cases} 1 & n = j \\ 0 & n \neq j \end{cases} \\
\hat{q}_j &= \frac{\bar{q}_j}{b_o} \\
k &= \frac{\omega b_o}{V_\infty} \\
A_{nj} &= \left[\frac{\rho b_o^3}{2M_n} \left(a_{nj} + i b_{nj} \right) + k^2 \delta_{nj} \right] \left(\frac{\omega_o}{\omega_n} \right)^2 \\
\lambda &= \left(\frac{\omega_o b_o}{V_\infty} \right)^2 (1 + ig)
\end{aligned}$$

Equation 3.17 can now be expressed:

$$\sum_{j=1}^{N} \left(A_{nj} - \lambda \delta_{nj} \right) \hat{q}_j = 0 \quad n = 1, 2, \ldots, N \tag{3.18}$$

This system of equations represents an eigenvalue problem. The eigenvalue solutions are complex. Define:

$$\lambda = \lambda_r + i\lambda_i = \left(\frac{\omega_o b_o}{V_\infty} \right)^2 + ig \left(\frac{\omega_o b_o}{V_\infty} \right)^2 \tag{3.19}$$

where $\lambda_r = (\omega_o b_o / V_\infty)^2$ is the real part of the eigenvalue and $\lambda_i = g(\omega_o b_o / V_\infty)^2$ is the imaginary part. The artificial damping ratio of each mode is the amount of damping the structure must possess to make the system neutrally stable. It is calculated from the imaginary part of Equation 3.19. The flutter speed occurs when g is equal to zero or at the minimum speed for which g is equal to a specified positive value. Determination of the flutter speed from the V-g graph is illustrated in Figure 3.1. The flutter speed is obtained from the real part of the eigenvalue:

$$V_f = \frac{\omega_o b_o}{\sqrt{\lambda_r}} \tag{3.20}$$

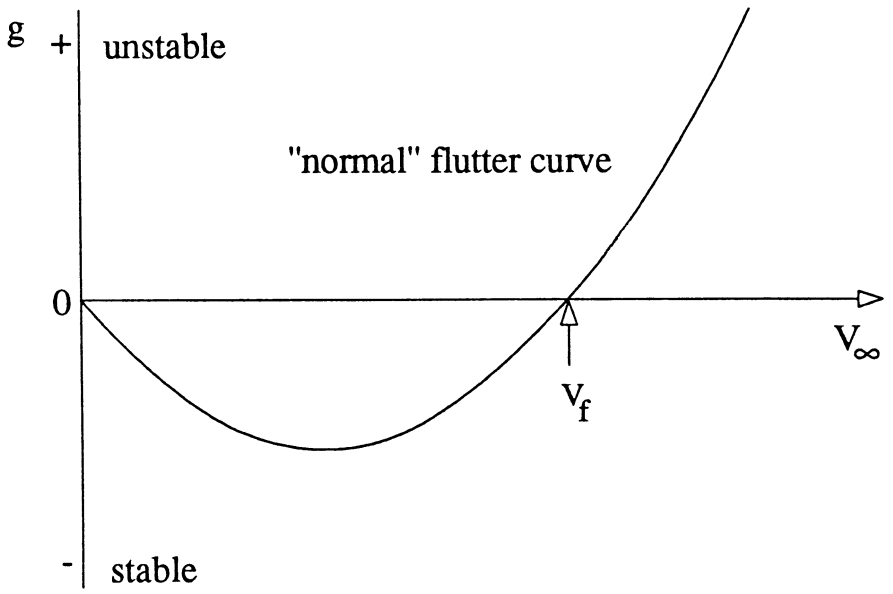

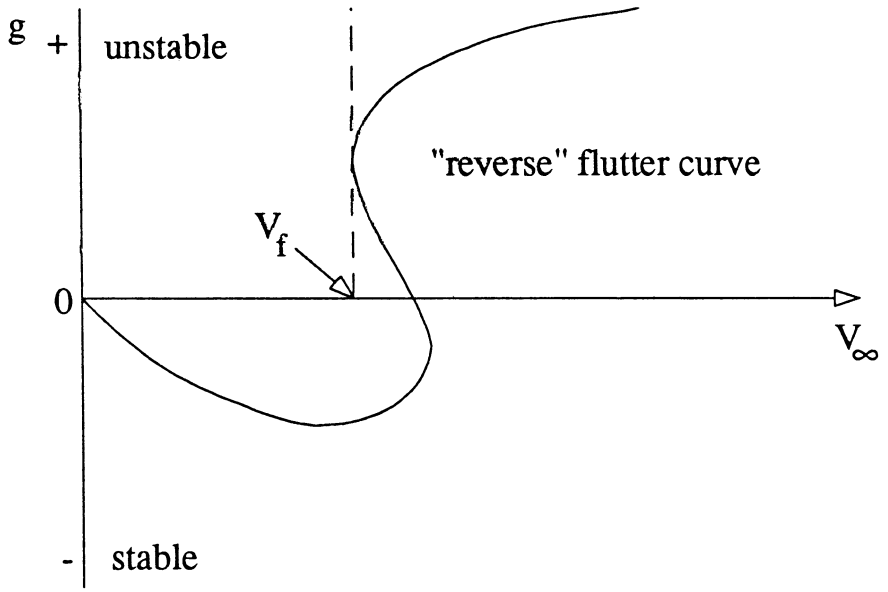

Figure 3.1: Examples of flutter curves.

Chapter 4

Analysis Procedure

The procedure used to perform the steady aerodynamic and aeroelastic analysis with USTSD is presented in this chapter. Both analysis were performed on a wing-fuselage representation of the Hawker 800XP business jet. The steady aerodynamic analysis is performed entirely with USTSD. The aeroelastic analysis procedure consisted of calculating the mode shapes, calculating the forcing function with USTSD and then inputing the forcing function into a code that solves the flutter equation. The USTSD procedure is detailed in Reference [12]. The analysis is summarized in this chapter.

4.1 Steady Analysis

Predictions of the Hawker 800 steady aerodynamic coefficients by the USTSD were evaluated against the wind tunnel data. The wind tunnel data was obtained for a fuselage, wing, nacelle and pylon configuration. A fuselage-wing configuration with the nacelle modelled as a solid body was analyzed in the USTSD. Based on the geometry data, the wing incidence is 2.0 degrees. The wing twist is -5.5 degrees.

Wind tunnel data was obtained at Mach numbers of 0.70, 0.75, 0.80 and 0.85. At each Mach number, the angle of attack was varied from 0.0 to 6.0 degrees by half degree increments. Sectional and total aircraft longitudinal coefficients were measured for all Mach numbers. Upper and lower surface wing pressure coefficients were measured at eight spanwise stations for all Mach numbers.

Aerodynamic coefficient predictions were performed with the USTSD at

Mach numbers of 0.70, 0.75, 0.80 and 0.85. Recognizing the limits of transonic small-disturbance theory, the angle of attack range examined was 0.0 to 3.0 degrees in half degree increments. The effects of applying the two-dimensional viscous boundary layer corrections and using a non-conservative formulation were also examined. Total aircraft longitudinal coefficients and wing pressure coefficients were then compared with the wind tunnel data.

4.2 Modal Analysis

The modal analysis of the wing was performed using NASTRAN 68. The fuselage was assumed rigid and neglected from the modal analysis. Only symmetric mode shapes were calculated. The analysis was restricted to mode shapes between 1 and 60 Hertz. In that range, eight mode shapes were calculated for the wing. The third and eighth mode shapes were neglected from the unsteady aerodynamic analysis. The third mode shape, the wing yawing mode, was neglected since it has negligible effect on the flutter solution. The shape of the eighth mode shape was judged too wavy to produce a realistic forcing function using USTSD and the corresponding frequency was too high to have any significant effect on the flutter conditions. The remaining six mode shapes are listed in Table 4.1 and presented in Figure 4.1.

A "beam" model was used to represent the wing in the NASTRAN finite element analysis (Figure 4.2). The model was composed of three components, the primary wing structure, the aileron and the aileron tab. All components were modeled with the CBEAM element. The aileron was connected to the wing with rigid bar elements. The aileron tab was connected to the aileron with elastic bar elements. To remove aileron tab modes from the solution, the stiffness of the elastic bar elements was increased until it was essentially rigid. The wing was fixed at the root grid point and allowed to deflect and rotate in all directions at all other grid points. Non structural damping was assumed for the analysis.

4.3 Unsteady Aerodynamic Analysis

The unsteady aerodynamic analysis was performed using USTSD. The input for this analysis was composed of geometric definition of the aircraft, mode shape deflections and flight conditions. The analysis was performed using

Table 4.1: Wing mode shape data.

Mode Shape	Generalized Mass $(lbf - s^2/in)$	Frequency (Hz)
1	3.2038E-01	5.99
2	3.9462E-01	17.38
3	3.0008E-01	28.46
4	1.8225E-01	32.45
5	4.4520E-01	39.14
6	3.6420E-01	44.90

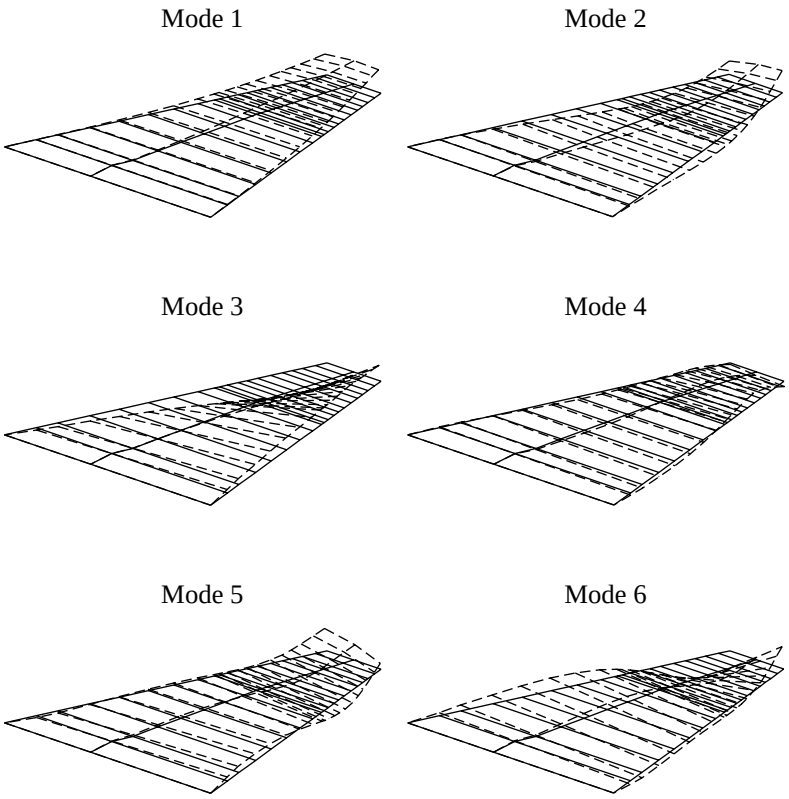

Figure 4.1: Wing mode shapes used in the USTSD analysis.

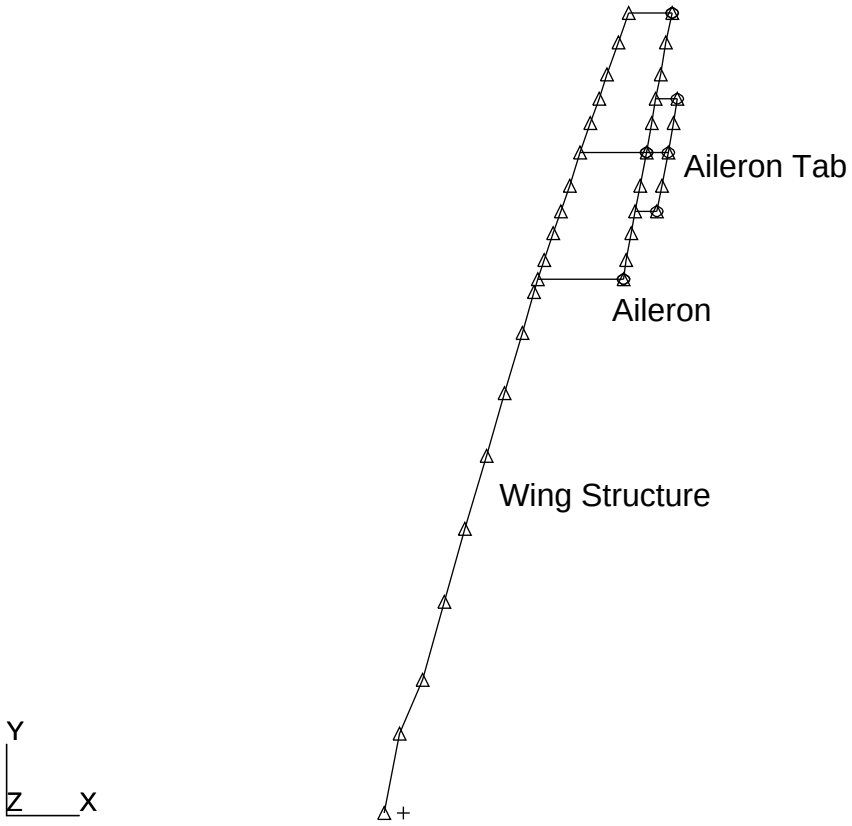

Figure 4.2: Beam model of the wing structure.

conservative and non-conservative differencing. A viscous flow correction was applied to all analysis. The geometry was defined by a wing-fuselage configuration. In the analysis, the fuselage was assumed rigid, included only to affect the wing pressure distribution. Modal data required for the analysis were the natural frequencies, deflection normalized mode shapes and the generalized mass. Modal deflections were interpolated to deflections on the aerodynamic grid using cubic spline interpolation. A symmetric analysis was performed, so the generalized mass listed in Table 4.1 is for half of the configuration. The solution was performed at several reduced frequency values for each Mach number. All analysis were performed with the configuration at 0 degrees angle of attack. The output for each reduced frequency value was used in the flutter analysis.

4.4 Flutter Analysis

The flutter analysis was performed using a code entitled FLUTTER. The input for this code is generated from the unsteady aerodynamic analysis performed using USTSD. The forcing function used in the flutter analysis is directly calculated in USTSD from the unsteady pressure coefficients. For each reduced frequency, the artificial damping required to make the system neutrally stable is calculated in FLUTTER. For a given reduced frequency, the density inputed into the solution can be varied until negative damping is obtained. Alternatively, for a given density, the flutter solution can be obtained for varying reduced frequency to obtain the point where negative damping is obtained. The method of varying the reduced frequency for a fixed density was used in FLUTTER.

Chapter 5

Steady Results & Analysis

Comparison of aerodynamic coefficients between the wind tunnel data and USTSD calculations are presented in this chapter. Pressure coefficients at root, mid and tip span stations are graphed at 3.0 degrees angle of attack for Mach numbers 0.70, 0.75, 0.80 and 0.85. Lift, drag and pitching moment coefficients are graphed against the angle of attack at Mach numbers 0.70, 0.75, 0.80 and 0.85. This section is concluded with a discussion of the results. Pressure coefficients at root, mid and tip span stations are graphed at 0.0 degrees angle of attack for Mach numbers 0.70 and 0.85 to substantiate the discussion of results. in the following, conservative and non-conservative formulations refer to solving Equations 2.4 and 2.5, respectively, in finite-difference forms.

5.1 Pressure Distributions

Calculated pressure coefficient distributions on the upper and lower surface of the wing at root, mid and tip span stations are compared with experimental data in this section. The definition of non-dimensional span in the experiment was with respect to the exposed wing span. The USTSD definition is with respect to the entire wing span. In the plots presented in this section, a conversion of the experimental span stations to correspond to the USTSD definition has been made.

5.1.1 Mach 0.70 Pressure Coefficients

Mach 0.70 pressure coefficients at 3.0 degrees angle of attack are presented first. The root pressure coefficients are plotted in Figure 5.1. On the forward portion of the upper surface, the calculated pressure coefficients are less than the data. On the aft portion of the upper surface, the calculated pressure coefficients are greater than the data. The calculated pressure coefficients along the lower surface are less than the data across the entire section.

The mid pressure coefficients are plotted in Figure 5.2. The calculated pressure coefficients on the upper surface correlate with the data except for the peak pressure. On the aft portion of the lower surface, the calculated pressure coefficients correlate well with the data. The pressure peak near the lower surface leading edge is not produced with the calculated pressure coefficients.

The tip pressure coefficients are plotted in Figure 5.3. The calculated pressure coefficients correlate well with the data on the aft portion of the upper surface. Near the leading edge, the calculated pressure coefficients are less than the data. On the lower surface, the pressure peak near the leading edge is not produced with the calculated pressure coefficients. The calculated pressure coefficients are greater than the data over the middle and aft portion of the lower surface.

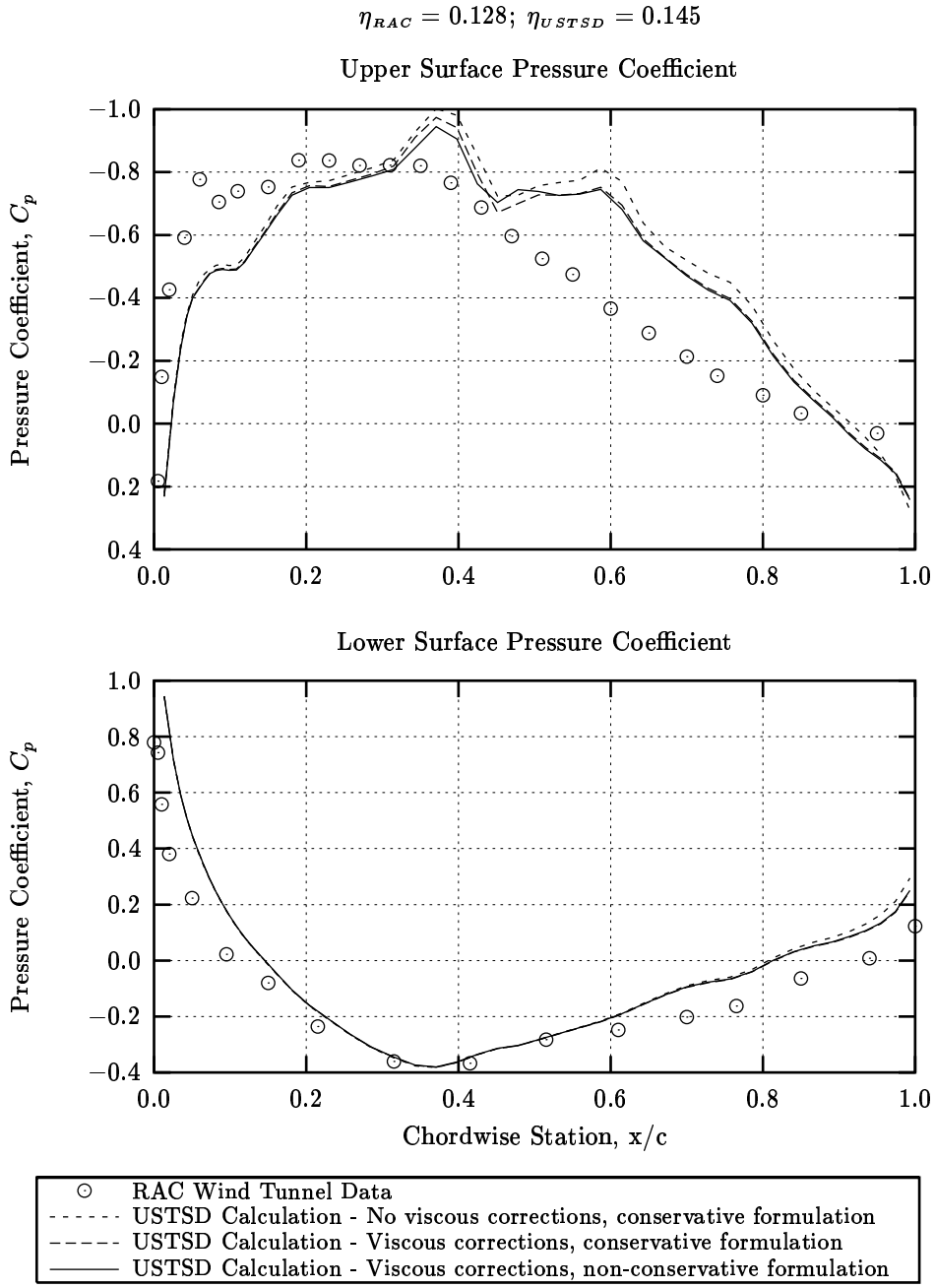

Figure 5.1: Root pressure coefficient at 0.70 Mach number, 3.0 degrees angle of attack, 3,000,000 Reynold's number.

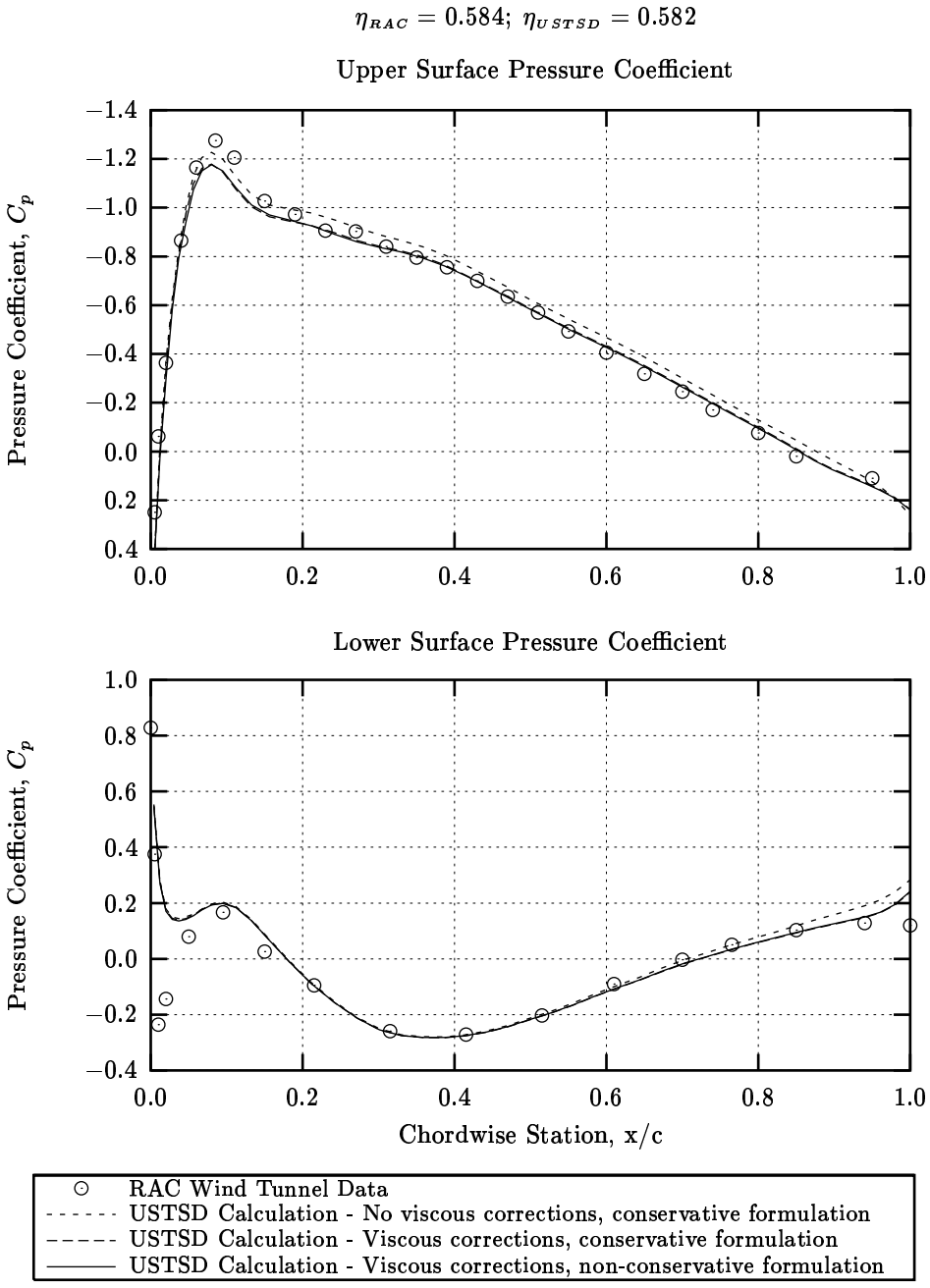

Figure 5.2: Mid pressure coefficient at 0.70 Mach number, 3.0 degrees angle of attack, 3,000,000 Reynold's number.

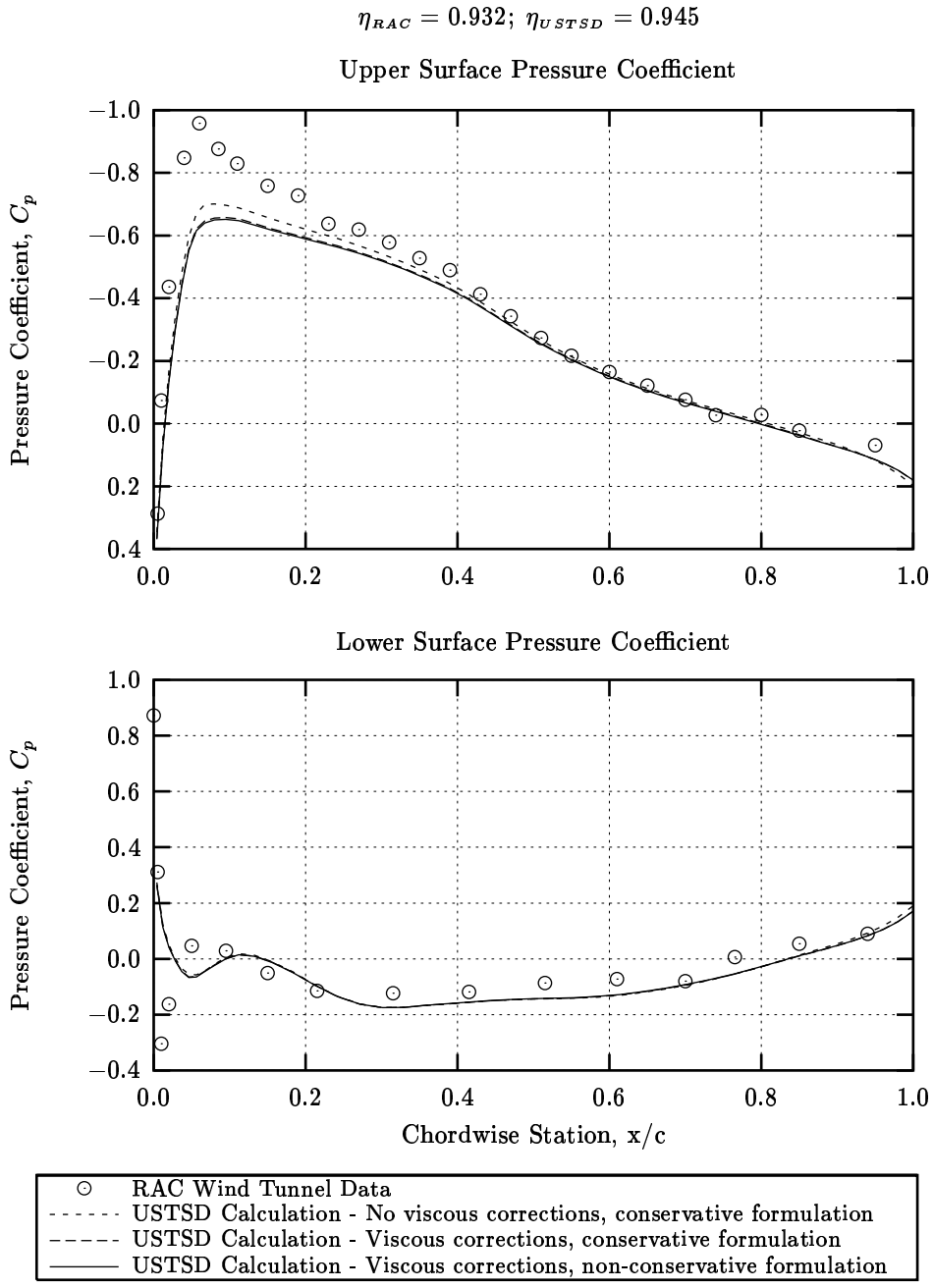

Figure 5.3: Tip pressure coefficient at 0.70 Mach number, 3.0 degrees angle of attack, 3,000,000 Reynold's number.

5.1.2 Mach 0.75 Pressure Coefficients

Mach 0.75 pressure coefficients at 3.0 degrees angle of attack are presented next. The root pressure coefficients are plotted in Figure 5.4. On the forward portion of the upper surface, the calculated pressure coefficients are less than the data. Variation in the calculated pressure coefficients on the forward upper surface does not correlate with the data. A shock is produced on the upper surface at approximately 0.75 chord for the conservative formulation. The non-conservative formulation produces the upper surface shock at approximately 0.65 chord. An upper surface shock is observed in the data at approximately 0.45 chord. The calculated pressure coefficients along the lower surface are less than the data across the entire section.

The mid pressure coefficients are plotted in Figure 5.5. Near the leading edge, the upper surface, calculated pressure coefficients correlate with the data. Through the middle section of the upper surface, the calculated pressure coefficients are less than the data. Pressure coefficients calculated using the conservative formulation produce a shock at approximately 0.6 chord. Aft of the shock on the upper surface, the calculated pressure coefficients are less than the data. The pressure coefficients calculated using the non-conservative formulation produce a shock at approximately 0.45 chord, which correlates with the data. The pressure coefficients also correlate with the data aft of the shock. On the lower surface near the leading edge, the pressure peak observed in the data is not produced with the calculated pressure coefficients. Aft of the leading edge, the calculated pressure coefficients correlate with the data.

The tip pressure coefficients are plotted in Figure 5.6. Near the leading edge, the calculated pressure coefficients are less than the data. The upper surface shock observed in the data at approximately 0.25 chord is not produced in the calculated data. Aft of the shock, the calculated pressure coefficients on the upper surface correlate with the data. The pressure peak near the leading edge on the lower surface is not produced with the calculated pressure coefficients. The calculated pressure coefficients of the middle and aft portion of the lower surface are greater than the data.

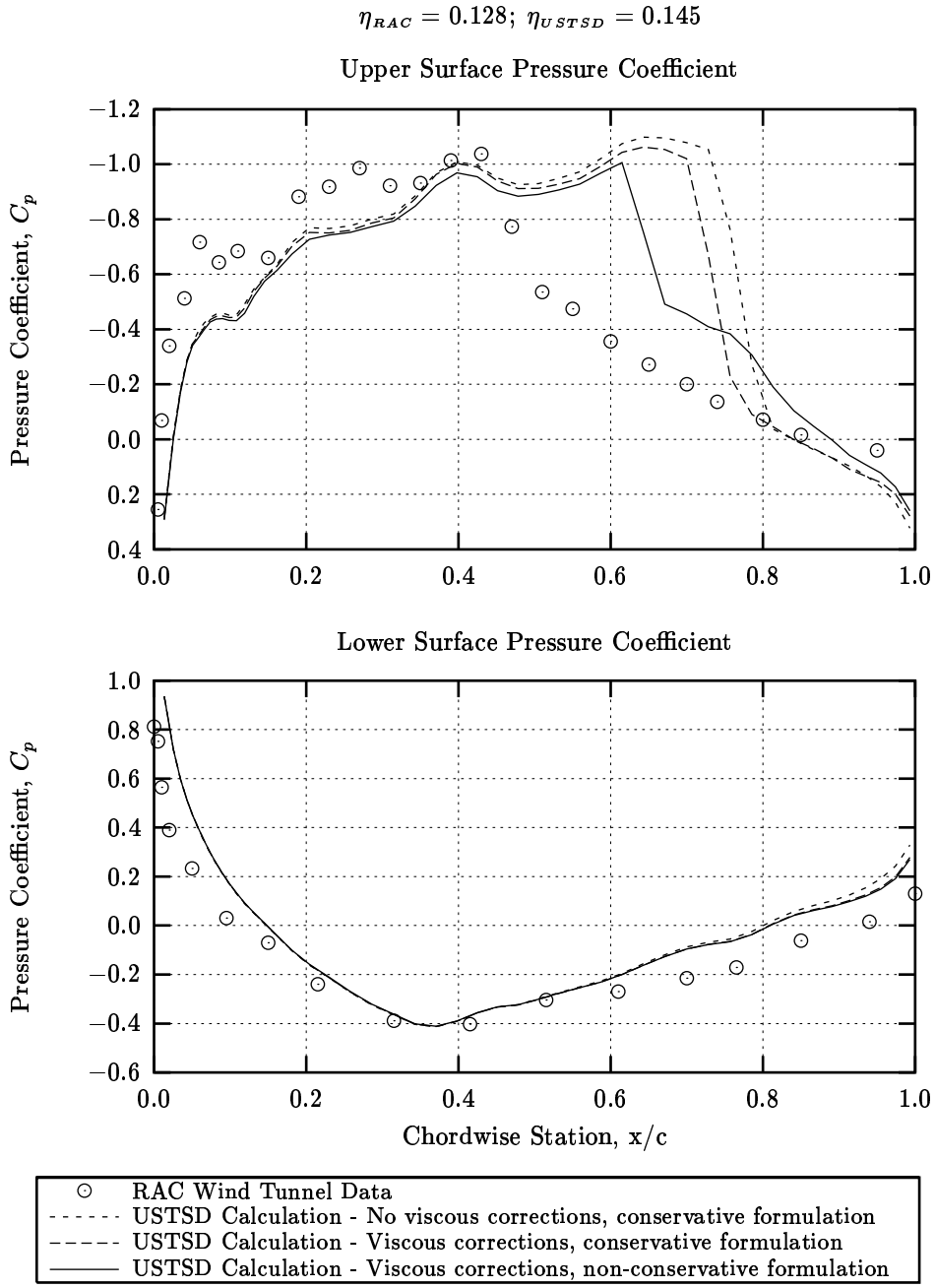

Figure 5.4: Root pressure coefficient at 0.75 Mach number, 3.0 degrees angle of attack, 3,000,000 Reynold's number.

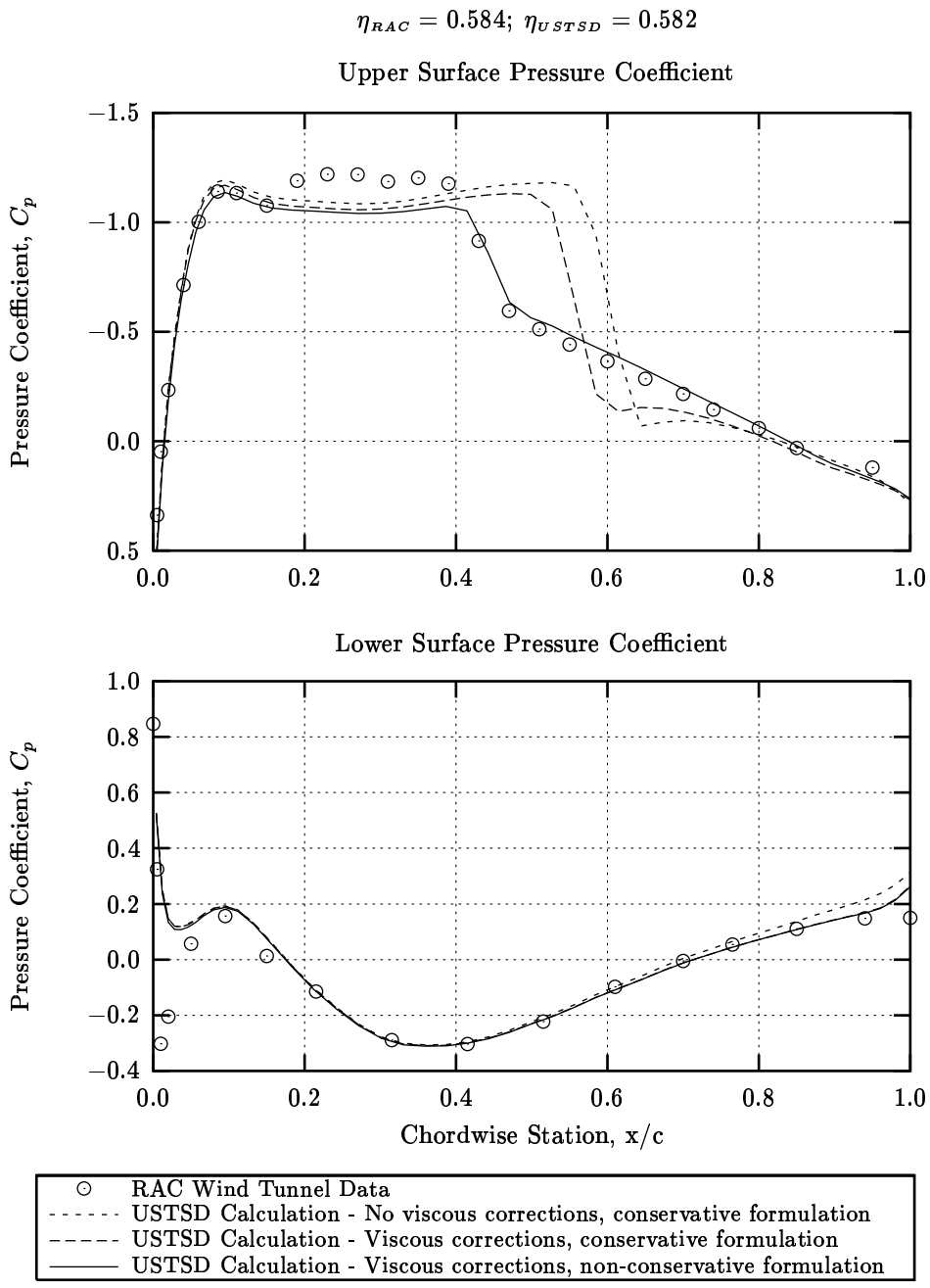

Figure 5.5: Mid pressure coefficient at 0.75 Mach number, 3.0 degrees angle of attack, 3,000,000 Reynold's number.

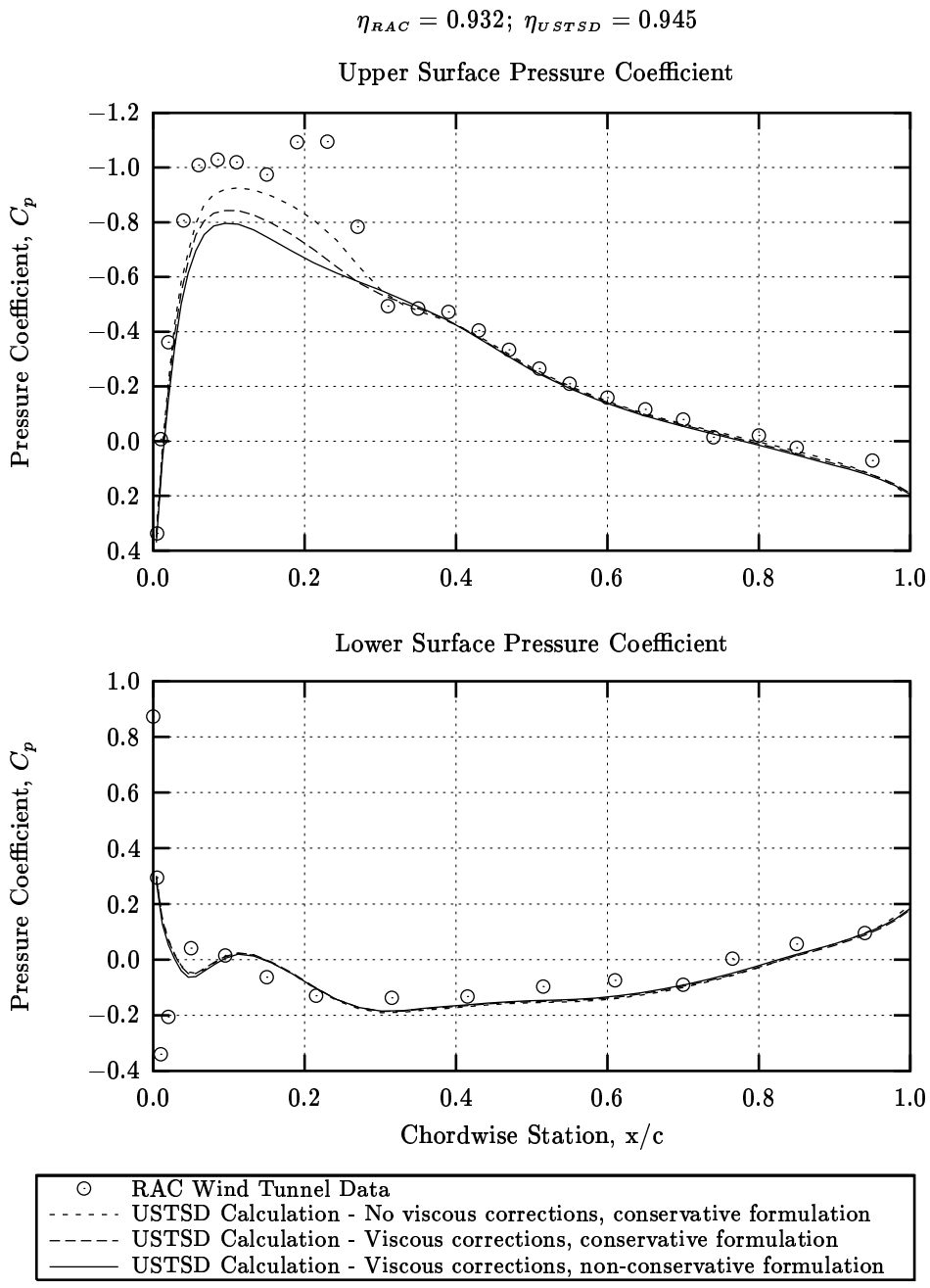

Figure 5.6: Tip pressure coefficient at 0.75 Mach number, 3.0 degrees angle of attack, 3,000,000 Reynold's number.

5.1.3 Mach 0.80 Pressure Coefficients

Mach 0.80 pressure coefficients at 3.0 degrees angle of attack are now presented. The root pressure coefficients are plotted in Figure 5.7. On the forward portion of the upper surface, the calculated pressure coefficients are less than the data. Further, the pressure coefficient variation does not correlate with the data. A shock is produced on the upper surface at approximately 0.92 chord for the conservative formulation and 0.78 chord for the non-conservative formulation. An upper surface shock is observed in the data at approximately 0.55 chord. The calculated pressure coefficients along the lower surface are less than the data across the entire section.

The mid pressure coefficients are plotted in Figure 5.8. A shock is observed in the data at approximately 0.42 chord on the upper surface. The calculated pressure coefficients correlate with the data from the leading edge to the shock. Pressure coefficients calculated using the conservative formulation produce a shock at approximately 0.85 chord. The pressure coefficients calculated using the non-conservative formulation produce a shock at approximately 0.58 chord. Aft of the shock on the upper surface, the calculated pressure coefficients are less than the data. On the lower surface near the leading edge, the pressure peak is not produced that is observed in the data. Aft of the leading edge, the calculated pressure coefficients are less than the data.

The tip pressure coefficients are plotted in Figure 5.9. A shock is observed in the data at approximately 0.37 chord. Using the conservative formulation, the calculated pressure coefficients correlate with the data forward of the shock, but do not produce a shock until approximately 0.55 chord. Using the non-conservative formulation, the calculated pressure coefficients are less than the data, but produce a shock at approximately the correct location. Aft of the shock, the conservative pressure coefficients are less than the data. The non-conservative pressure coefficients correlate with the data aft of the shock. The pressure peak near the leading edge on the lower surface is not produced in the calculated data. The calculated pressure coefficients of the middle and aft portion of the lower surface are greater than the data.

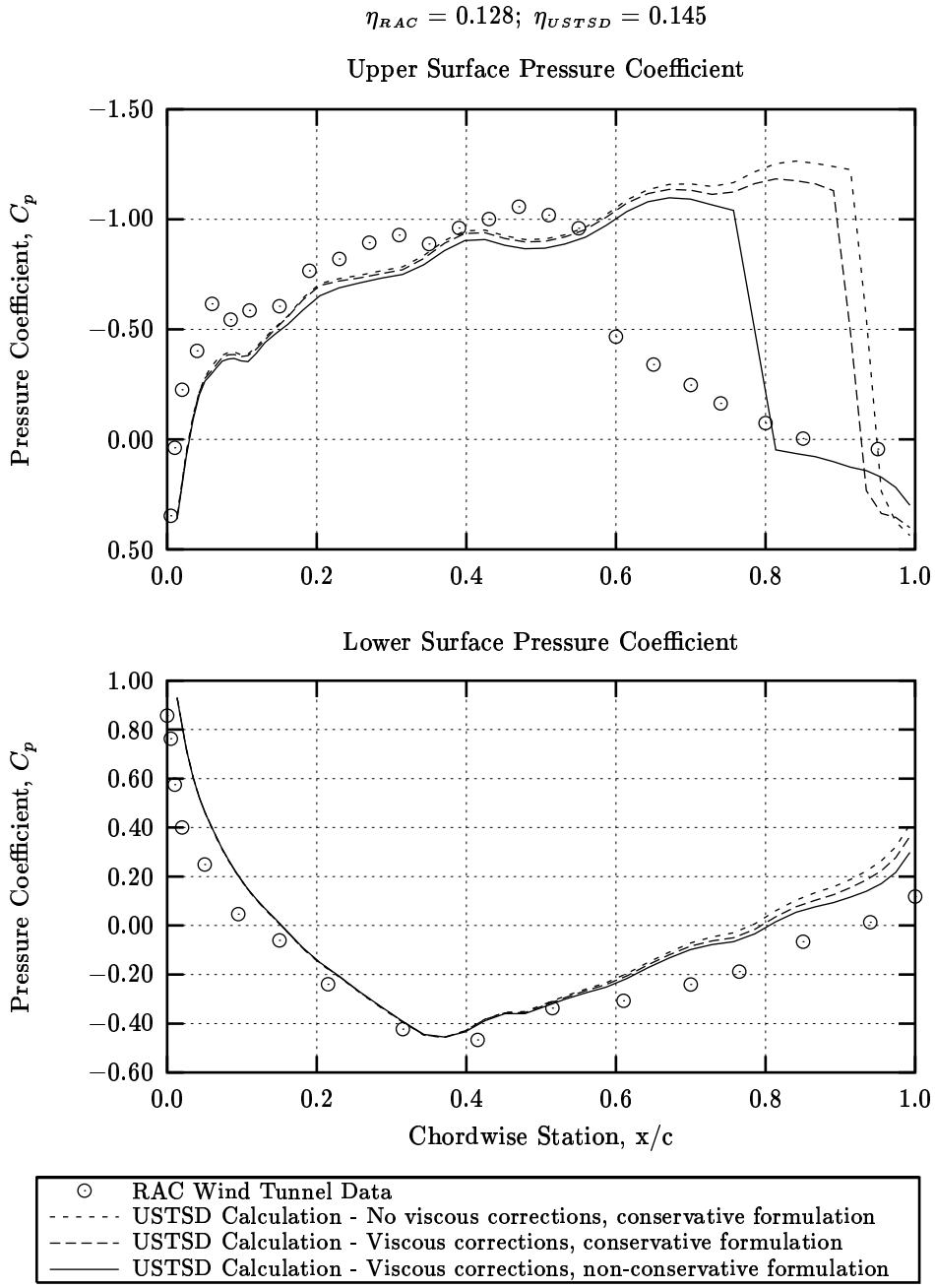

Figure 5.7: Root pressure coefficient at 0.80 Mach number, 3.0 degrees angle of attack, 3,000,000 Reynold's number.

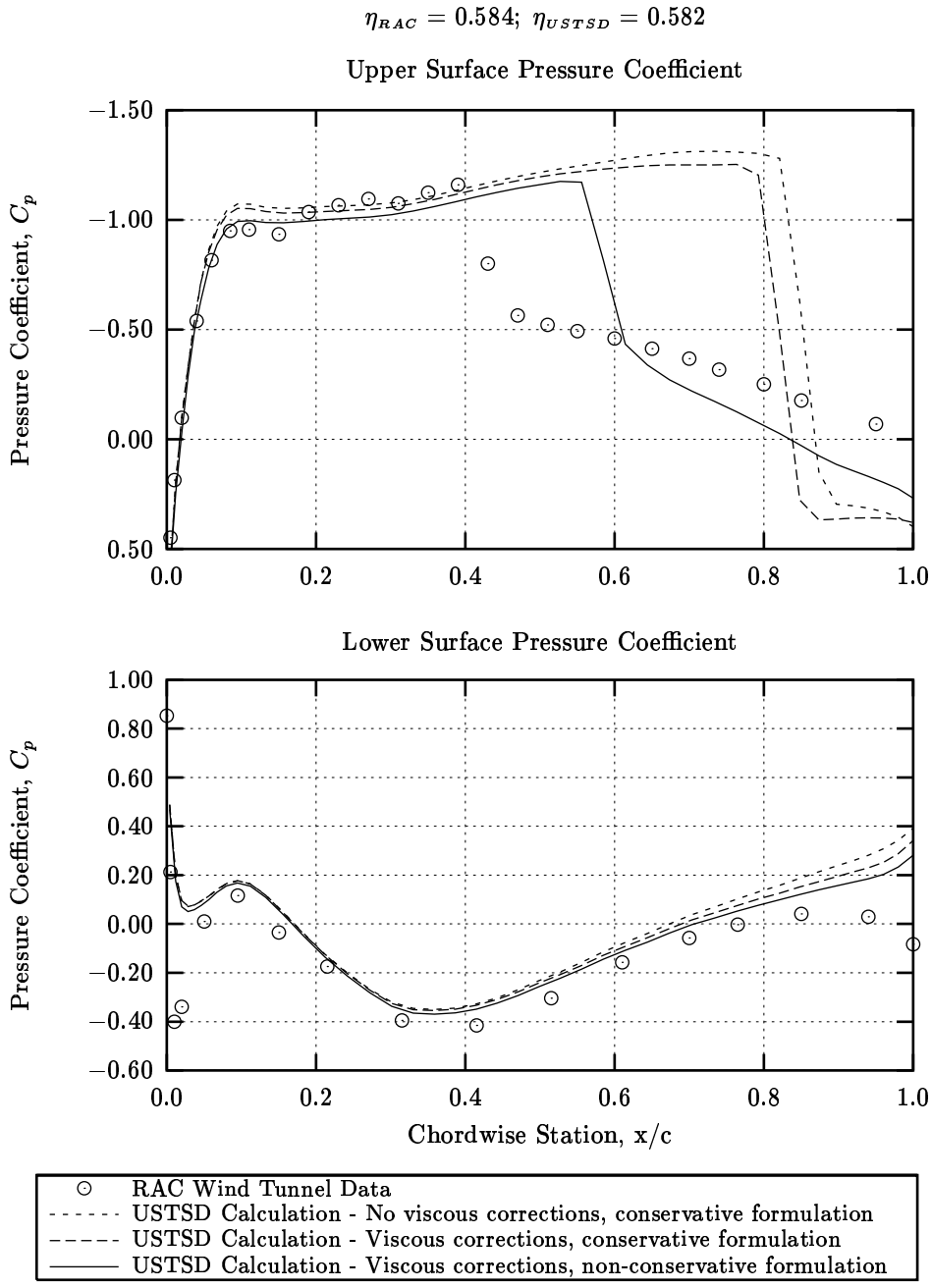

Figure 5.8: Mid pressure coefficient at 0.80 Mach number, 3.0 degrees angle of attack, 3,000,000 Reynold's number.

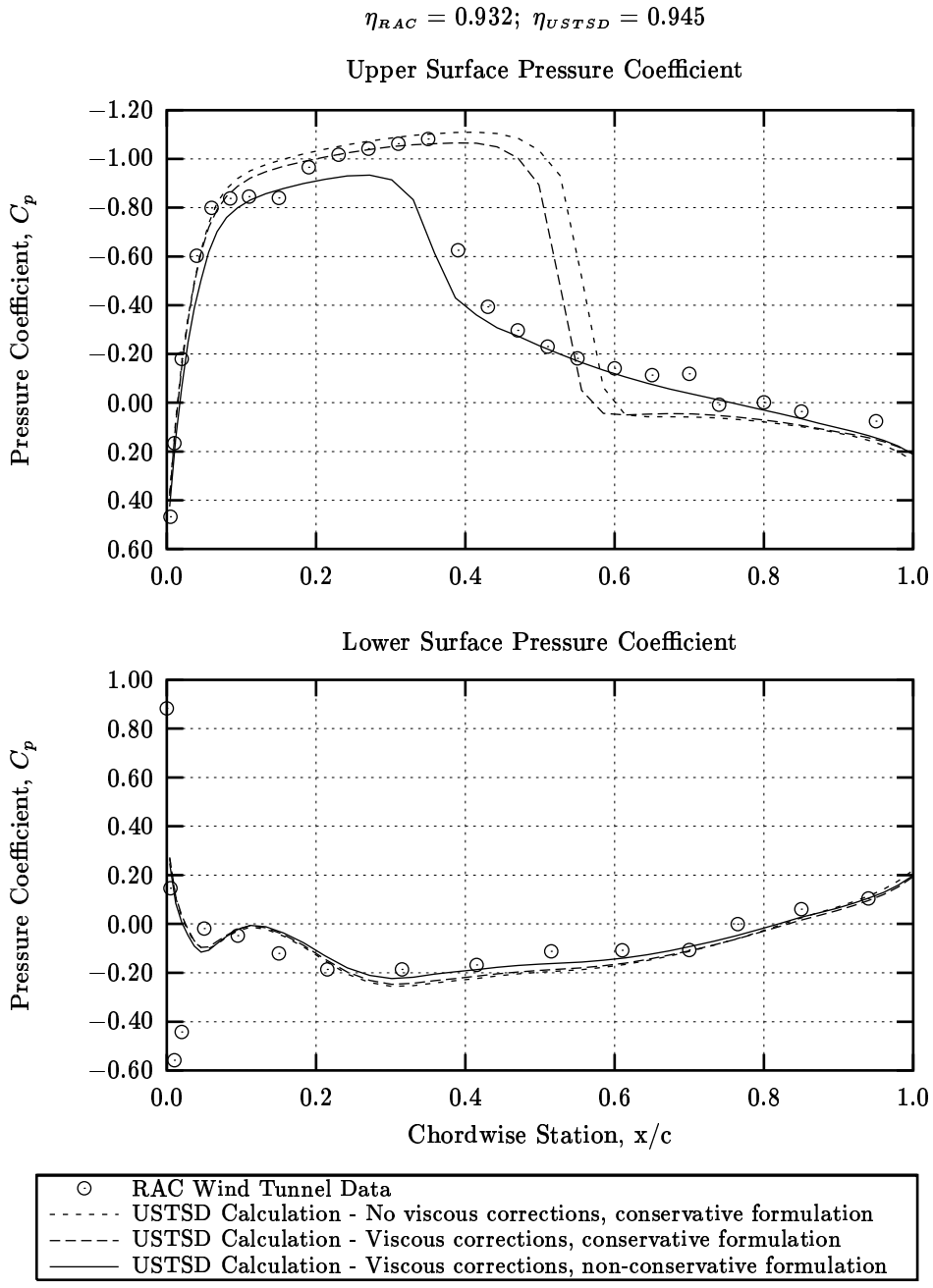

Figure 5.9: Tip pressure coefficient at 0.80 Mach number, 3.0 degrees angle of attack, 3,000,000 Reynold's number.

5.1.4 Mach 0.85 Pressure Coefficients

Mach 0.85 pressure coefficients at 3.0 degrees angle of attack are presented last. The root pressure coefficients are plotted in Figure /reffig:cp10. On the forward portion of the upper surface, the calculated pressure coefficients are less than the data. Further, the variation does not correlate with the data. A shock is produced on the upper surface at approximately 0.97 chord for the conservative formulation and 0.85 chord for the non-conservative formulation. An upper surface shock is observed in the data at approximately 0.62 chord. The calculated pressure coefficients along the lower surface are less than the data across the entire section. Variations on the aft portion of the lower surface in the calculated pressure coefficients are not observed in the data.

The mid pressure coefficients are plotted in Figure 5.11. A shock is observed in the data at approximately 0.48 chord on the upper surface. The calculated pressure coefficients correlate with the data from the leading edge to the shock. Pressure coefficients calculated using the conservative formulation produce a shock at approximately 0.97 chord. The pressure coefficients calculated using the non-conservative formulation produce a shock at approximately 0.73 chord. The calculated pressure coefficients are less than the data aft of the shock. On the lower surface near the leading edge, the pressure peak is not produced that is observed in the data. Aft of the leading edge, the calculated pressure coefficients are less than the data.

The tip pressure coefficients are plotted in Figure 5.12. A shock is observed in the data at approximately 0.40 chord. Using the conservative formulation, the calculated pressure coefficients are greater than the data forward of the shock, but do not produce a shock until approximately 0.9 chord. Using the non-conservative formulation, the calculated pressure coefficients correlate with the data, but do not produce a shock until approximately 0.5 chord. Aft of the shock, the calculated pressure coefficients are less than the data. The pressure peak near the leading edge on the lower surface is not produced in the calculated data. The calculated pressure coefficients of the middle and aft portion of the lower surface are greater than the data.

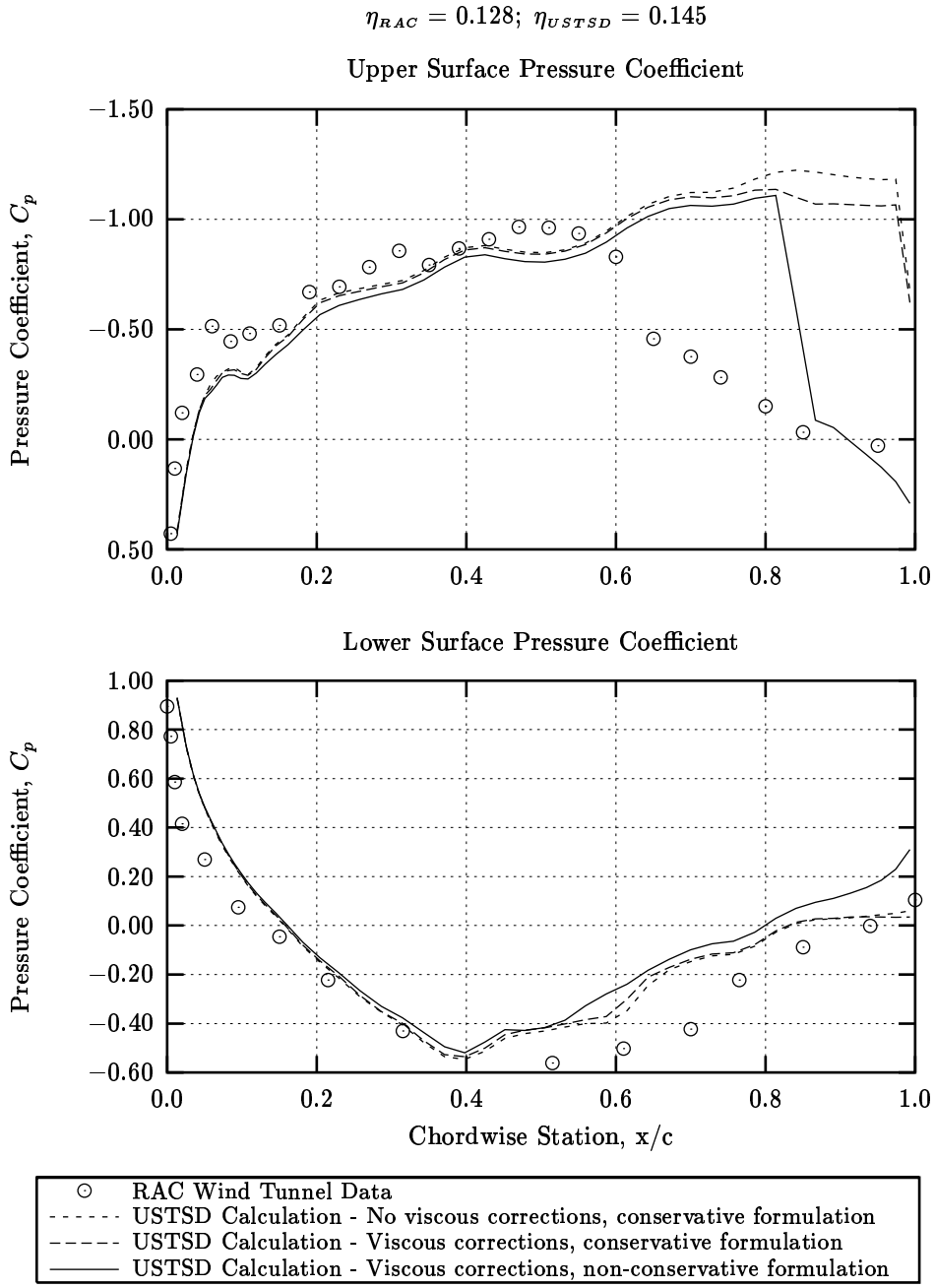

Figure 5.10: Root pressure coefficient at 0.85 Mach number, 3.0 degrees angle of attack, 3,000,000 Reynold's number.

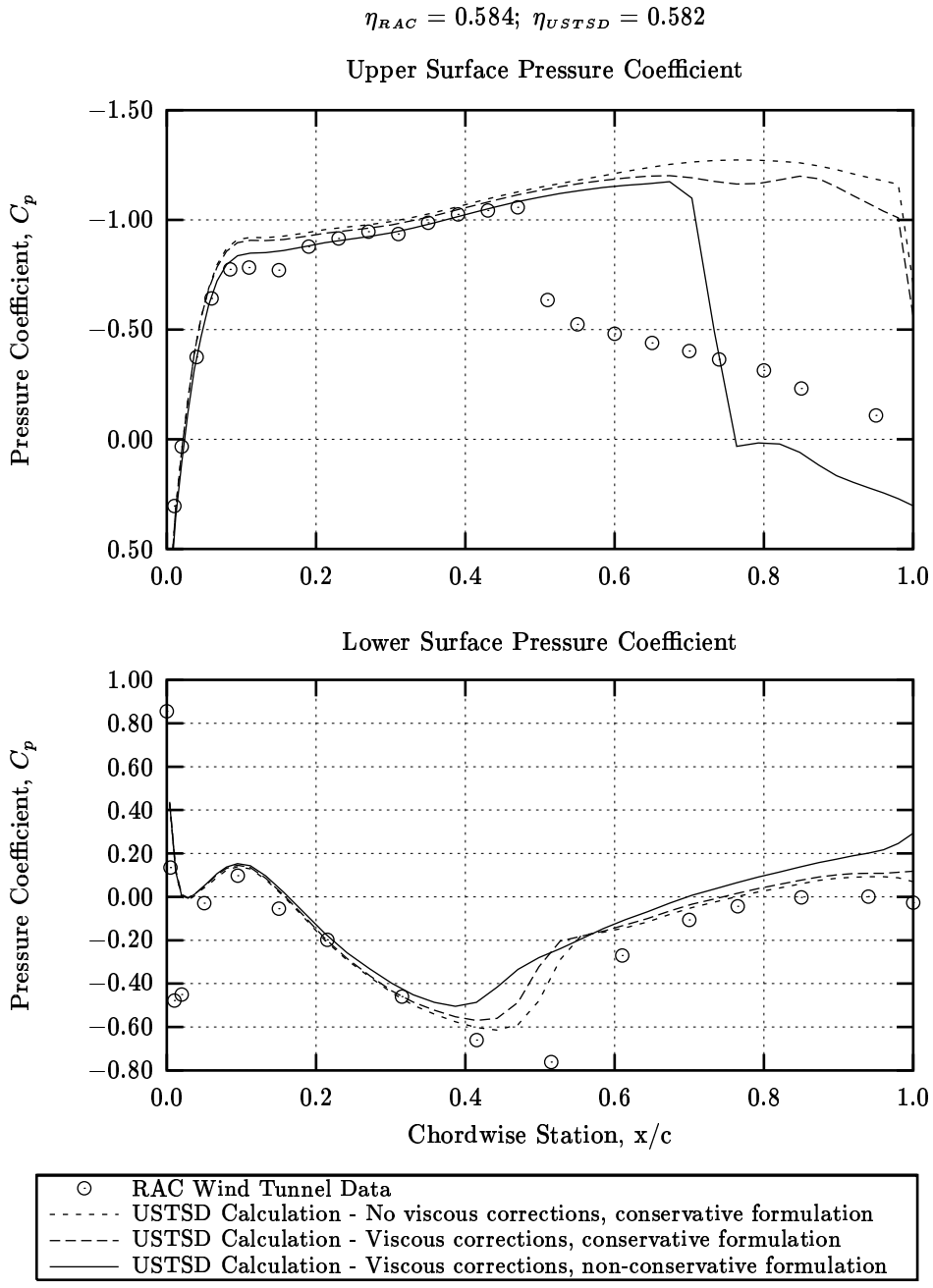

Figure 5.11: Mid pressure coefficient at 0.85 Mach number, 3.0 degrees angle of attack, 3,000,000 Reynold's number.

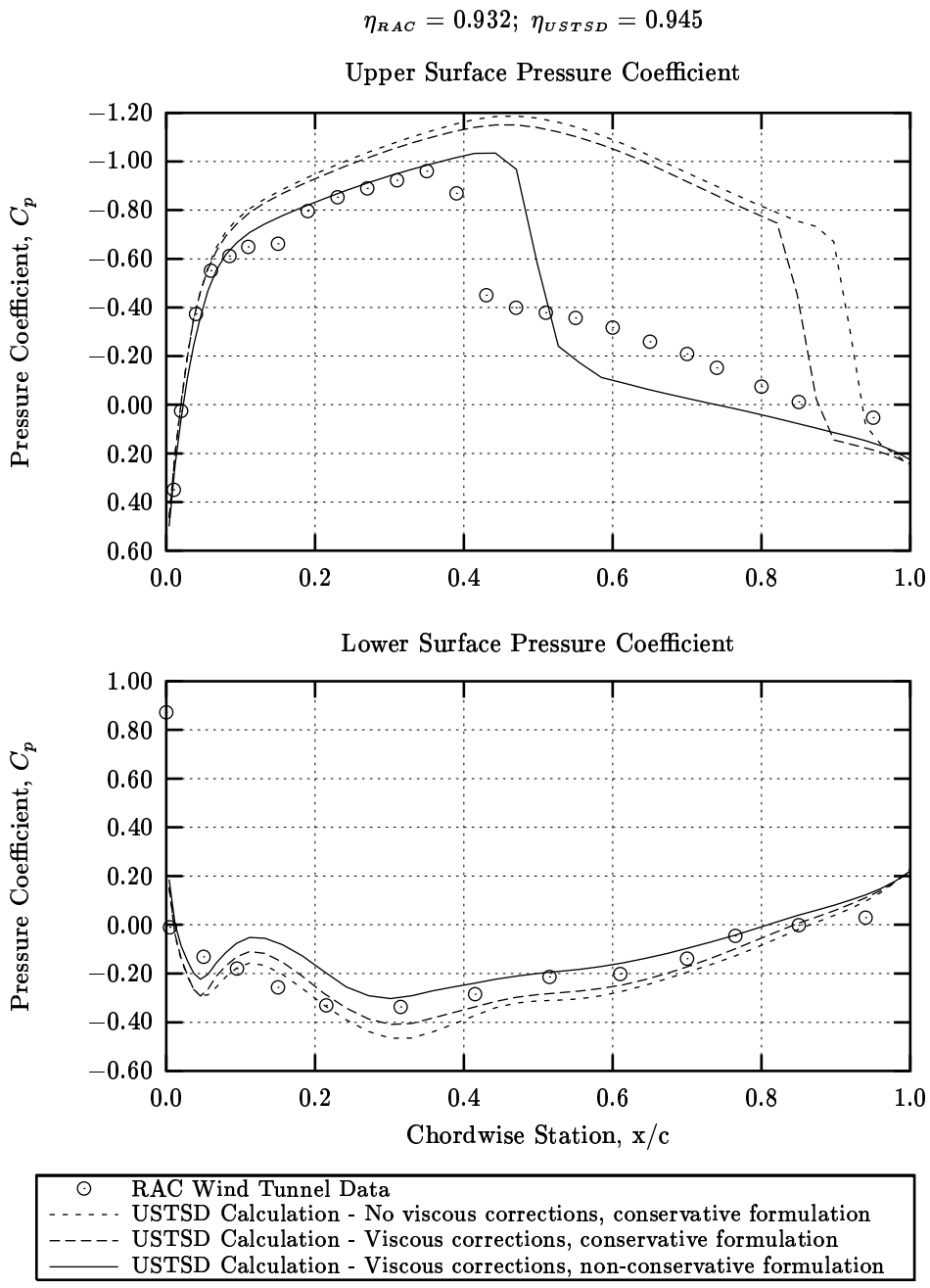

Figure 5.12: Tip pressure coefficient at 0.85 Mach number, 3.0 degrees angle of attack, 3,000,000 Reynold's number.

5.2 Lift Coefficient

In Figure 5.13, the lift coefficient is presented for 0.70 Mach number. The calculated lift coefficient with no viscous corrections using the conservative formulation is approximately 0.08 greater than the data across the entire angle of attack range. With viscous corrections, the conservative formulation at 0.0 degrees angle of attack calculates the lift coefficient 0.06 greater than the data. The difference decreases to approximately 0.0 at 3.0 degrees angle of attack. No improvement in lift coefficient is observed with viscous corrections using the non-conservative formulation.

The lift coefficient for 0.75 Mach number is presented in Figure 5.14. Using the conservative formulation with no viscous corrections, the calculated lift coefficient is 0.10 greater than the data. Applying viscous corrections but still using the conservative formulation, the difference between the calculation and the data is reduced. At 0.0 degrees angle of attack, the difference is 0.07. At 3.0 degrees angle of attack, the difference reduces to 0.03. There is no improvement in lift coefficient at 0.0 degrees angle of attack using viscous corrections with the non-conservative formulation. The difference improves with angle of attack, decreasing to 0.0 at 3.0 degrees angle of attack.

The lift coefficient for 0.80 Mach number is presented in Figure 5.15. Using no viscous corrections with the conservative formulation, the calculated lift coefficient is 0.20 higher than the data at 0.0 degrees angle of attack. The difference increases with angle of attack to 0.32 at 3.0 degrees angle of attack. Applying viscous corrections with the conservative formulation decreases the difference between the data and the calculation. The difference between the calculation and the data is 0.17 at 0.0 degrees angle of attack and 0.25 at 3.0 degrees angle of attack. At 0.0 degrees angle of attack, the lift coefficient calculated using non-conservative differencing and viscous corrections is 0.10 higher than the data. The difference decreases to 0.05 at 3.0 degrees angle of attack.

In Figure 5.16, the lift coefficient at 0.85 Mach number is plotted. The largest discrepancy is observed with the conservative formulation, when no viscous corrections are applied. At 0.0 degrees angle of attack, the lift coefficient is calculated to be 0.36 greater than the data. The difference increases with angle of attack to 0.45 at 3.0 degrees angle of attack. By using viscous corrections with the conservative formulation, the lift coefficient is decreased by approximately 0.02 from no viscous corrections across the entire angle of attack range. At 0.0 degrees angle of attack with viscous corrections

and non-conservative differencing, the lift coefficient is calculated to be 0.16 greater than the data. The difference increases with angle of attack to 0.20 at 3.0 degrees angle of attack.

The lift curve slope of the data from the wind tunnel increases with Mach numbers 0.70 to 0.75. It then decreases with Mach numbers 0.75 to 0.85. The lift curve slope from the USTSD calculation using the conservative formulation increases with Mach number 0.70 to 0.80, then decreases with Mach number 0.80 to 0.85. Using the non-conservative formulation, the lift curve slope increases with Mach number 0.70 to 0.85. Lift curve slope variation with Mach number is listed in Table 5.1. The angle of attack for zero lift coefficient of the data from the wind tunnel varies with Mach number. The angle of attack for zero lift coefficient from the USTSD calculation also varies with Mach number. Listed in Table 5.2 is the variation of the angle of attack for zero lift coefficient with Mach number. As has been shown in comparing the pressure distributions, one reason for the discrepancy in prediction with data is the inability of the code to predict the correct locations of the shock wave, resulting in lower pressure over most of the upper surface. As a result, the lift is higher.

Table 5.1: Variation of lift curve slope with Mach number.

Lift Curve Slope	Mach Number 0.70	0.75	0.80	0.85
Wind Tunnel Data	5.83	6.47	5.97	5.06
No viscous corrections, conservative formulation	5.01	6.07	7.98	6.57
Viscous corrections, conservative formulation	4.81	5.66	7.38	6.66
Viscous corrections, non-conservative formulation	4.71	5.12	5.14	5.58

Table 5.2: Variation of zero lift coefficient angle of attack with Mach number.

Angle of Attack for Zero Lift Coefficient	Mach Number 0.70	0.75	0.80	0.85
Wind Tunnel Data	-0.68	-0.61	-0.73	-0.21
No viscous corrections, conservative formulation	-1.7	-1.6	-2.1	-3.3
Viscous corrections, conservative formulation	-1.5	-1.4	-1.9	-3.0
Viscous corrections, non-conservative formulation	-1.5	-1.5	-1.9	-1.9

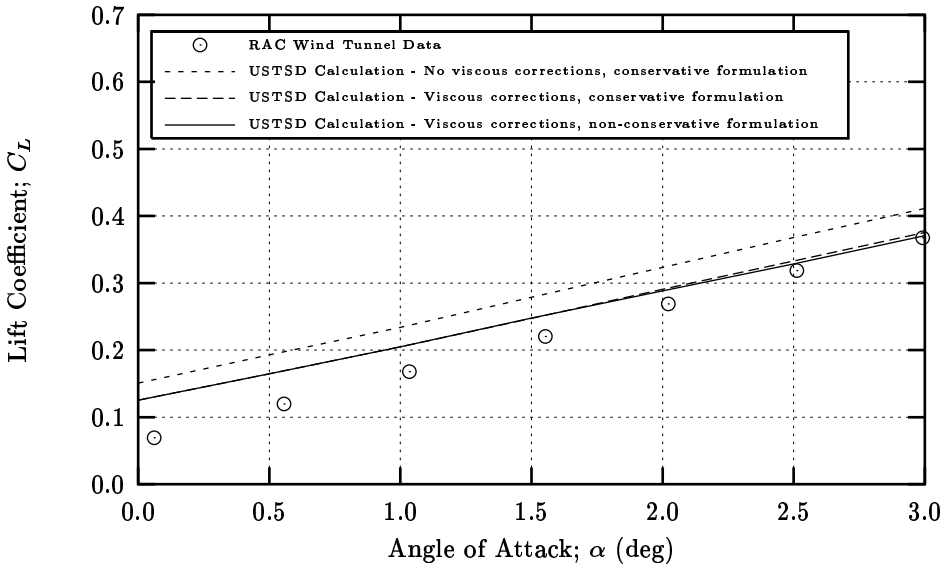

Figure 5.13: Lift coefficient at 0.70 Mach number, 3,000,000 Reynold's number, for a Hawker 800 fuselage-wing-nacelle configuration.

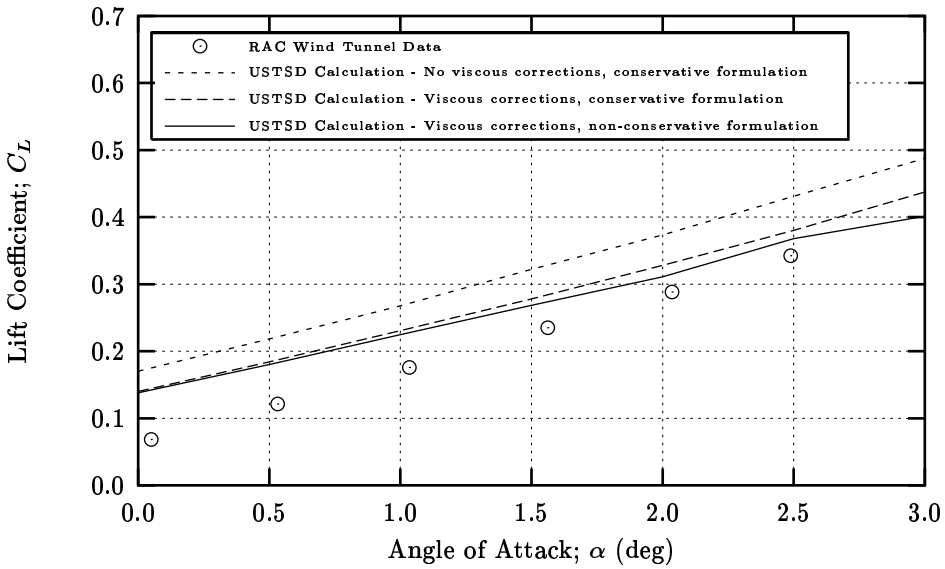

Figure 5.14: Lift coefficient at 0.75 Mach number, 3,000,000 Reynold's number, for a Hawker 800 fuselage-wing-nacelle configuration.

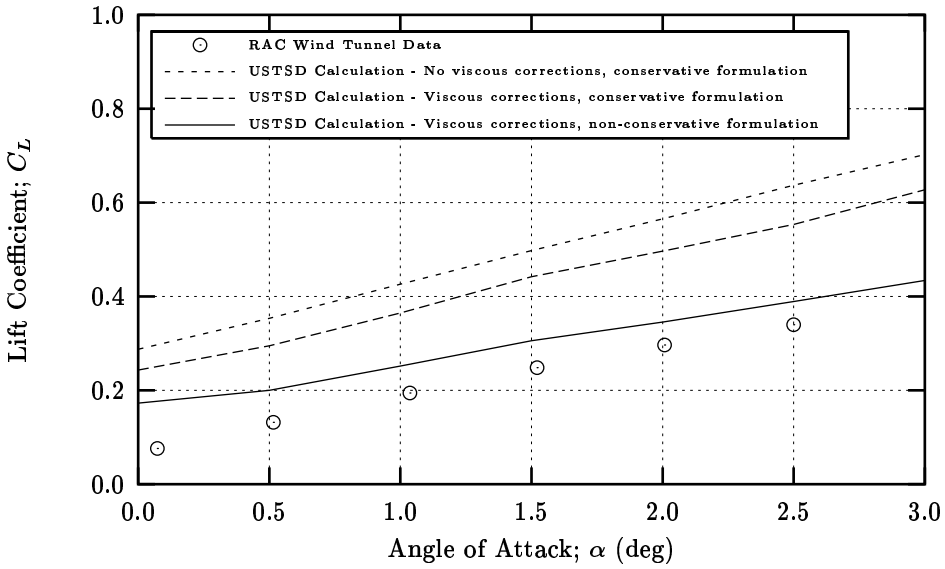

Figure 5.15: Lift coefficient at 0.80 Mach number, 3,000,000 Reynold's number, for a Hawker 800 fuselage-wing-nacelle configuration.

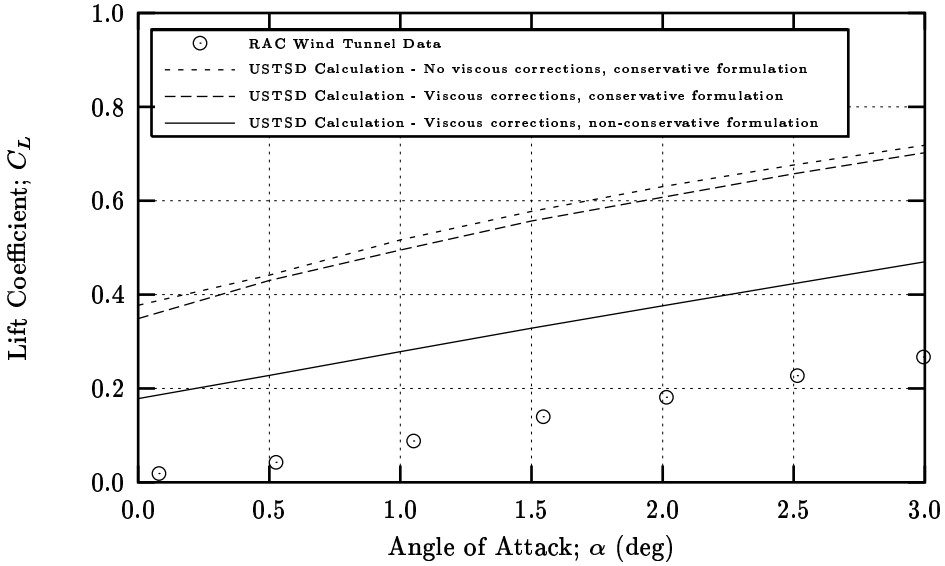

Figure 5.16: Lift coefficient at 0.85 Mach number, 3,000,000 Reynold's number, for a Hawker 800 fuselage-wing-nacelle configuration.

5.3 Drag Coefficient

The drag coefficient at 0.70 Mach number is presented in Figure 5.17. Using no viscous corrections and the conservative formulation, the calculated drag coefficient is 0.0026 to 0.0044 greater than the wind tunnel data. Applying the viscous corrections decreases the error between the calculation and the data. With viscous corrections, the error ranges from 0.005 to 0.008. No improvements in the error between the calculation and the data are gained by applying viscous corrections with the non-conservative formulation.

The 0.75 Mach number drag coefficient is presented in Figure 5.18. With no viscous corrections, using the conservative formulation, the drag coefficient varies from 0.011 to 0.016 greater then the data. Using the conservative formulation with viscous corrections reduces the calculated drag coefficient, resulting in the drag coefficient calculated 0.008 higher than the data over the entire alpha range. The drag coefficient calculated using the non-conservative formulation with viscous corrections is not improved over the conservative formulation at low angles of attack. At higher angles of attack, the drag coefficient is improved, reducing the error to approximately 0.005 greater than the data.

The 0.80 Mach number drag coefficient is plotted in Figure 5.19. The calculated drag coefficient with no viscous corrections using the conservative formulation is from 0.026 to 0.054 greater than the data. With viscous corrections, the calculated drag coefficient is from 0.019 to 0.039 greater than the data. The least error between the calculation and the data is achieved by using the non-conservative formulation with viscous corrections, resulting in drag coefficients from 0.01 to 0.005 greater than the data. The main difference in these calculations arises from the predicted wave drag.

In Figure 5.20, the 0.85 Mach number drag coefficient is presented. Using the conservative formulation with no viscous corrections, the calculated drag coefficient is 0.035 to 0.062 greater than the data. This error is greater than the error observed at 0.70, 0.75 and 0.80 Mach numbers. By applying viscous corrections, the calculated drag coefficient is reduced by approximately 0.005. The smallest error between the data and the calculation is observed by applying viscous corrections and using the non-conservative formulation. With these calculation options, the largest error is 0.009 to 3.0 degrees angle of attack.

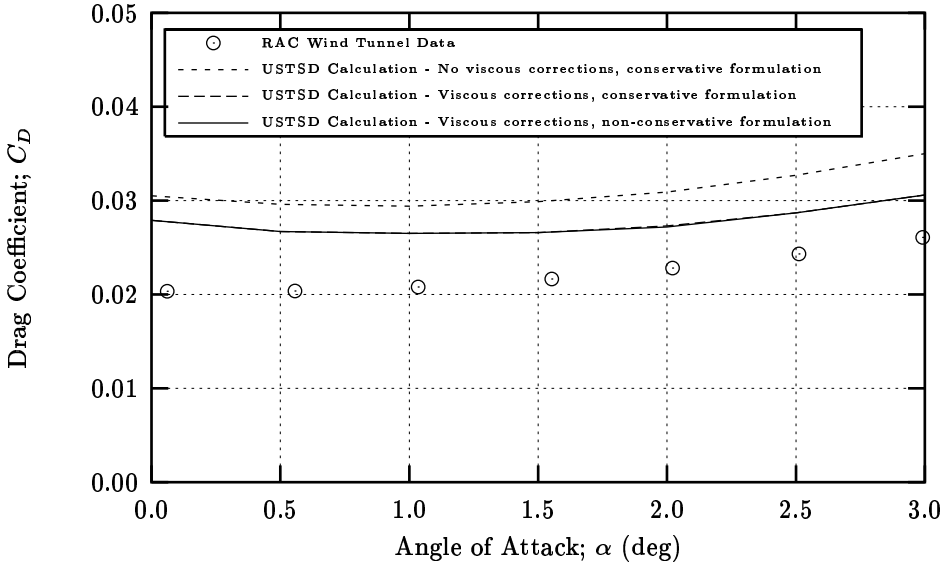

Figure 5.17: Drag coefficient at 0.70 Mach number, 3,000,000 Reynold's number, for a Hawker 800 fuselage-wing-nacelle configuration.

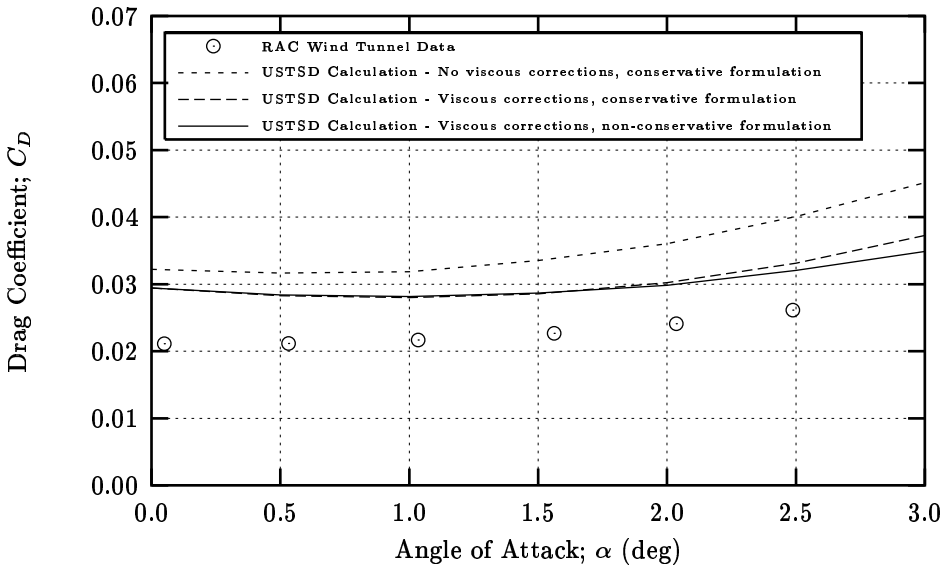

Figure 5.18: Drag coefficient at 0.75 Mach number, 3,000,000 Reynold's number, for a Hawker 800 fuselage-wing-nacelle configuration.

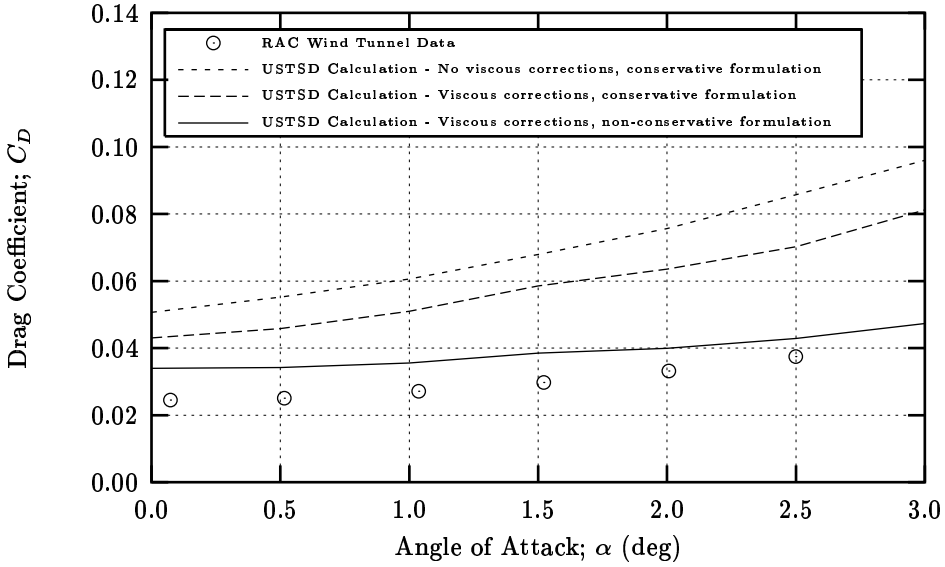

Figure 5.19: Drag coefficient at 0.80 Mach number, 3,000,000 Reynold's number, for a Hawker 800 fuselage-wing-nacelle configuration.

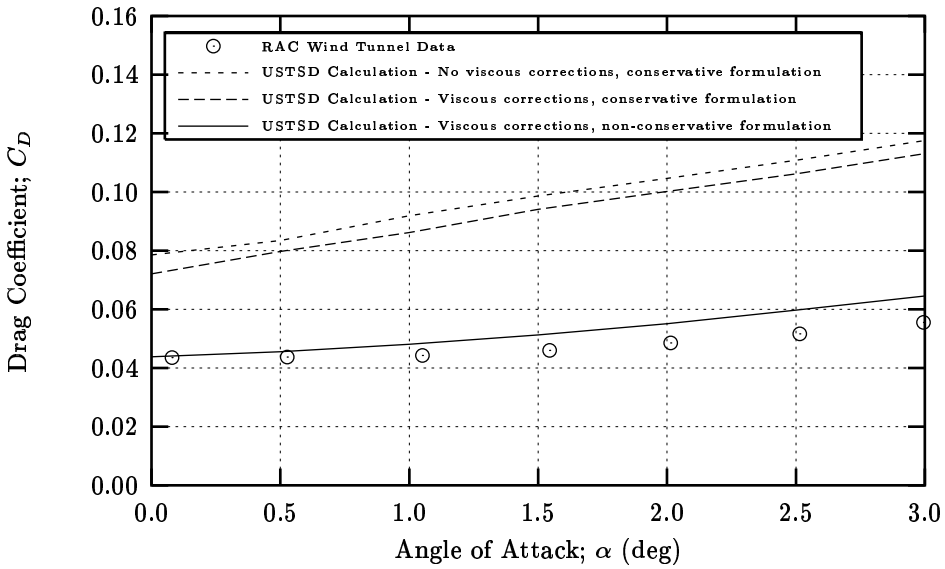

Figure 5.20: Drag coefficient at 0.85 Mach number, 3,000,000 Reynold's number, for a Hawker 800 fuselage-wing-nacelle configuration.

5.4 Pitching Moment Coefficient

The pitching moment coefficient at 0.70 Mach number is presented in Figure 5.21. The calculation performed using the conservative formulation with no viscous corrections is greater than the data by approximately 0.008. Applying viscous corrections increases the difference by approximately 0.006 using both the conservative and non-conservative formulation.

The 0.75 Mach number pitching moment coefficient is plotted in Figure 5.22. The calculated lift coefficient using the conservative formulation with no viscous corrections is higher than the data by approximately 0.003. The difference increases with the application of viscous corrections. At 0.0 degrees angle of attack the error is 0.009 and 0.016 at 3.0 degrees angle of attack. At low angles of attack, a decrease in pitching moment coefficient of approximately 0.0003 is observed between the conservative and non-conservative formulation. At 3.0 degrees angle of attack, this difference is reversed.

Plotted in Figure 5.23 is the pitching moment coefficient for 0.80 Mach number. The pitching moment coefficient calculated using no viscous corrections and the conservative formulation is from 0.042 to 0.12 less than the data. Applying viscous corrections positively increases the pitching moment coefficient by approximately 0.03 over the case with no viscous corrections. The calculated pitching moment coefficient is 0.015 greater than the data when viscous corrections are applied with the non-conservative formulation.

The pitching moment coefficient at 0.85 Mach number is illustrated in Figure 5.24. The pitching moment coefficient calculated using no viscous corrections and the conservative formulation is form 0.19 to 0.23 less than the data. Applying viscous corrections positively increases the pitching moment coefficient by approximately 0.15 over the case with no viscous corrections. The calculated pitching moment coefficient is approximately 0.05 lower than the data when viscous corrections are applied with the non-conservative formulation. To summarize, the prediction of pitching moment is very much affected by the predicted shock position and strength. In general, the predicted shock is more aft and its strength is larger when the conservative formulation is used as compared with the non-conservative formulation.

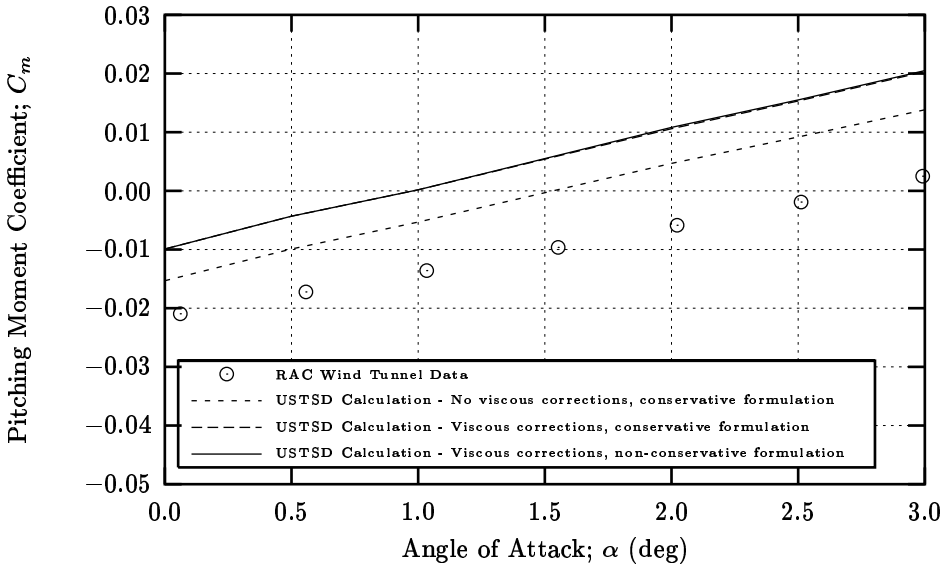

Figure 5.21: Pitching moment coefficient at 0.70 Mach number, 3,000,000 Reynold's number, for a Hawker 800 fuselage-wing-nacelle configuration.

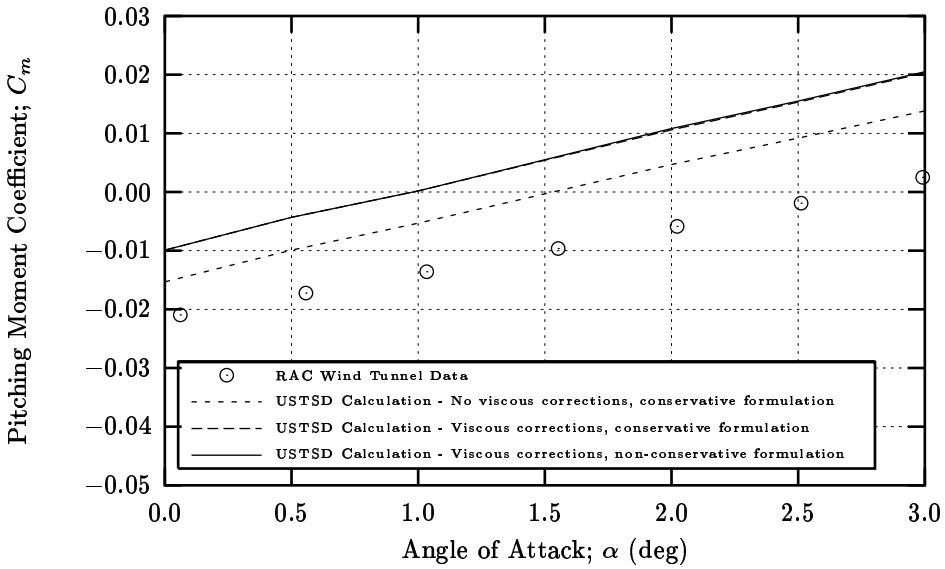

Figure 5.22: Pitching moment coefficient at 0.75 Mach number, 3,000,000 Reynold's number, for a Hawker 800 fuselage-wing-nacelle configuration.

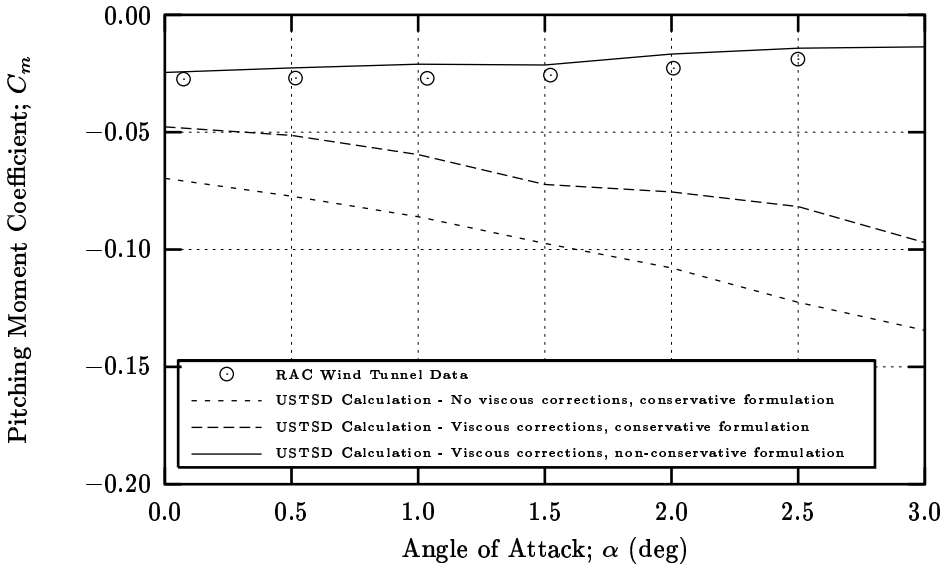

Figure 5.23: Pitching moment coefficient at 0.80 Mach number, 3,000,000 Reynold's number, for a Hawker 800 fuselage-wing-nacelle configuration.

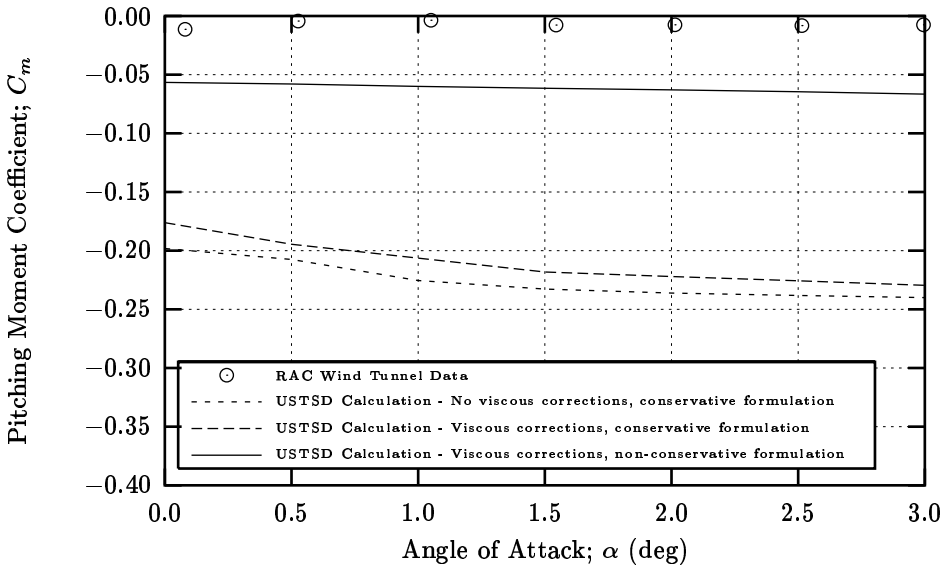

Figure 5.24: Pitching moment coefficient at 0.85 Mach number, 3,000,000 Reynold's number, for a Hawker 800 fuselage-wing-nacelle configuration.

5.5 Analysis of Predicted Results

At all Mach numbers, the lift coefficient calculated with USTSD is greater than the wind tunnel data lift coefficient. The calculated drag coefficient is also greater than the data drag coefficient. The calculated pitching moment coefficient is more positive than the data at 0.70 and 0.75 Mach numbers. It is more negative at 0.80 and 0.85 Mach numbers. The difference between the total aerodynamic force coefficients calculated with USTSD and measured in the wind tunnel can be attributed to:

- Wing-fuselage interference effects at the root
- Strong shock-boundary layer interactions.
- Nacelle and pylon effects

The wing-fuselage interference effects are not determined correctly at the root section in USTSD. Near the leading edge of the root, the calculated pressure coefficients on the upper surface are less than the data at all Mach numbers. Calculated aft pressure coefficients on the upper surface are greater than the data. Along the entire lower surface, the calculated pressure coefficients are less than the data. These discrepancies between the calculated pressure coefficients and the wind tunnel data are also observed at 0.0 degrees angle of attack, illustrated in Figure 5.25 and Figure 5.28. The experimental pressure coefficients exhibit a variation that is not matched well by the calculated pressure coefficients.

The effect of the nacelle modelled as a solid body was neglible on the results. The body boundary conditions used in the analysis are derived from slender body theory. Considering the body as a source-sink pair, no circulation is generated by the body. Therefore, the body has little effect in the far-field. Another aspect of the nacelle results is the grid generation. Since the nacelle is modeled in a separate fine grid domain from the wing, nacelle effects on the wing must be transmitted by the course grid. The nacelle may not be properly covered by the course grid to transmit the effects. This results in a weak coupling between the wing and the nacelle, where the wing influences the nacelle, but the nacelle has no influence on the wing.

The root, mid and tip pressure coefficients at 0.0 degrees angle of attack, 0.70 Mach number are presented in Figures 5.25 through 5.27. No strong

shocks are observed in the data. Consequently, the calculated pressure coefficients correlate with the data. The root, mid and tip pressure coefficients at 0.0 degrees angle of attack, 0.85 Mach number are presented in Figures 5.28 through 5.30. At the root and mid sections, shocks are observed on both the upper and lower surfaces. On the upper surface, the calculated shock position is aft of the shock position observed in the data in Figures 5.28 and 5.29. The calculated shock position on the root lower surface is forward of the shock position observed in the data in Figure 5.28. No shocks in the data are observed on the mid, lower surface, although the USTSD calculates one, illustrated in Figure 5.29. The error in calculated pressure near the lower surface leading edge coupled with the error in calculated shock position account for the lift and pitching moment coefficient discrepancies.

The calculated mid and tip pressure coefficients near the leading edge, on the lower surface do not produce the pressure peak observed in the data. At 0.70 and 0.75 Mach numbers (Figure 5.1 - Figure 5.6), the upper surface calculated pressure coefficients at the tip are less than the data. At 0.80 and 0.85 Mach numbers (Figure 5.7 - Figure 5.12), the upper surface calculated pressure coefficients at the tip correlate with the data.The error in calculated pressure near the lower surface leading edge coupled with the error in calculated shock position account for the lift and pitching moment coefficient discrepancies. When no viscous corrections are performed during the USTSD solution, the drag coefficient should be less than the data. The skin friction coefficient for all inviscid calculations was approximately 0.013, which is less than the data. The remaining component of drag is the pressure component. Since the lower surface, leading edge pressure coefficients calculated with the USTSD were smaller in magnitude than the data, the calculated leading edge thrust would be less. Lower leading edge thrust would result in higher pressure drag, accounting for the error observed in the calculated drag coefficient.

The presence of a strong shock in the flow reduces the correspondence between the experimental and calculated pressure coefficients. At Mach numbers 0.75, 0.80 and 0.85, the presence of a shock is observed in the data. When the shock is strong, the shock position calculated with the USTSD is aft of the observed shock position. Prediction of the shock being too aft may result from not modeling the vorticity and entropy effects associated with strong shocks (Ref. [1]) or from strong shock-boundary layer interactions (Ref. [4]). In the USTSD code, the effects of vorticity and entropy in calculating the pressure coefficient have been included. Therefore, the main deficiency in

the code is the inability in accounting for the strong shock-boundary layer interaction that affects not only the shock position, but atlso the pressure distribution ahead and behind the shock. The discrepancy between the conservative and non-conservative solution can be attributed to the generation of mass after the shock in the non-conservative solution (Ref. [15]). Interactions between the shock and the boundary layer can relieve the required pressure jump across the shock, resulting in a shock the is forward of the theoretically predicted position. The mass generated using the non-conservative formulation mimics the effect of the boundary layer after a strong shock, resulting in a solution that corresponds more closely to experiment than the conservative solution.

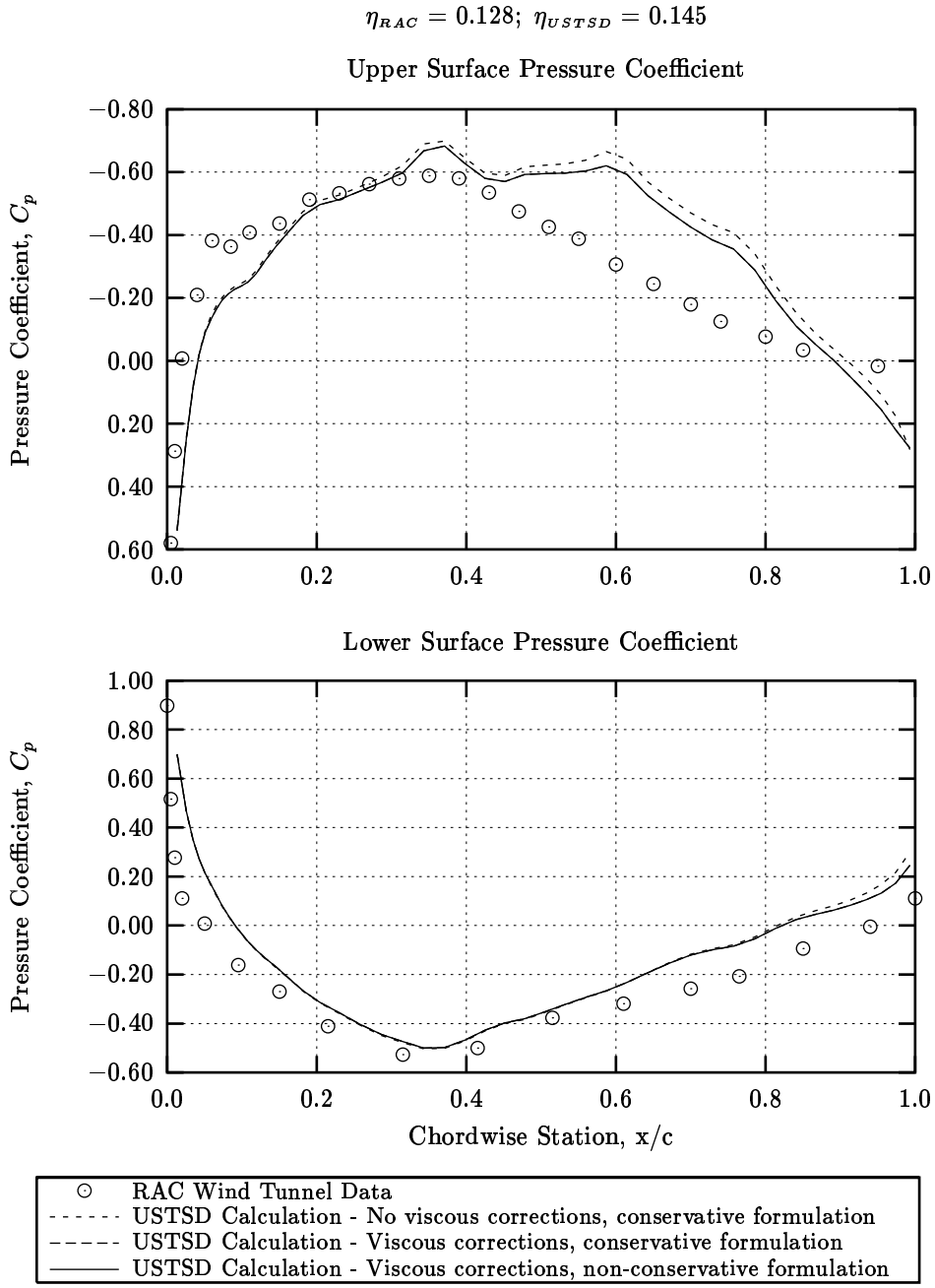

Figure 5.25: Root pressure coefficient at 0.70 Mach number, 0.0 degrees angle of attack, 3,000,000 Reynold's number.

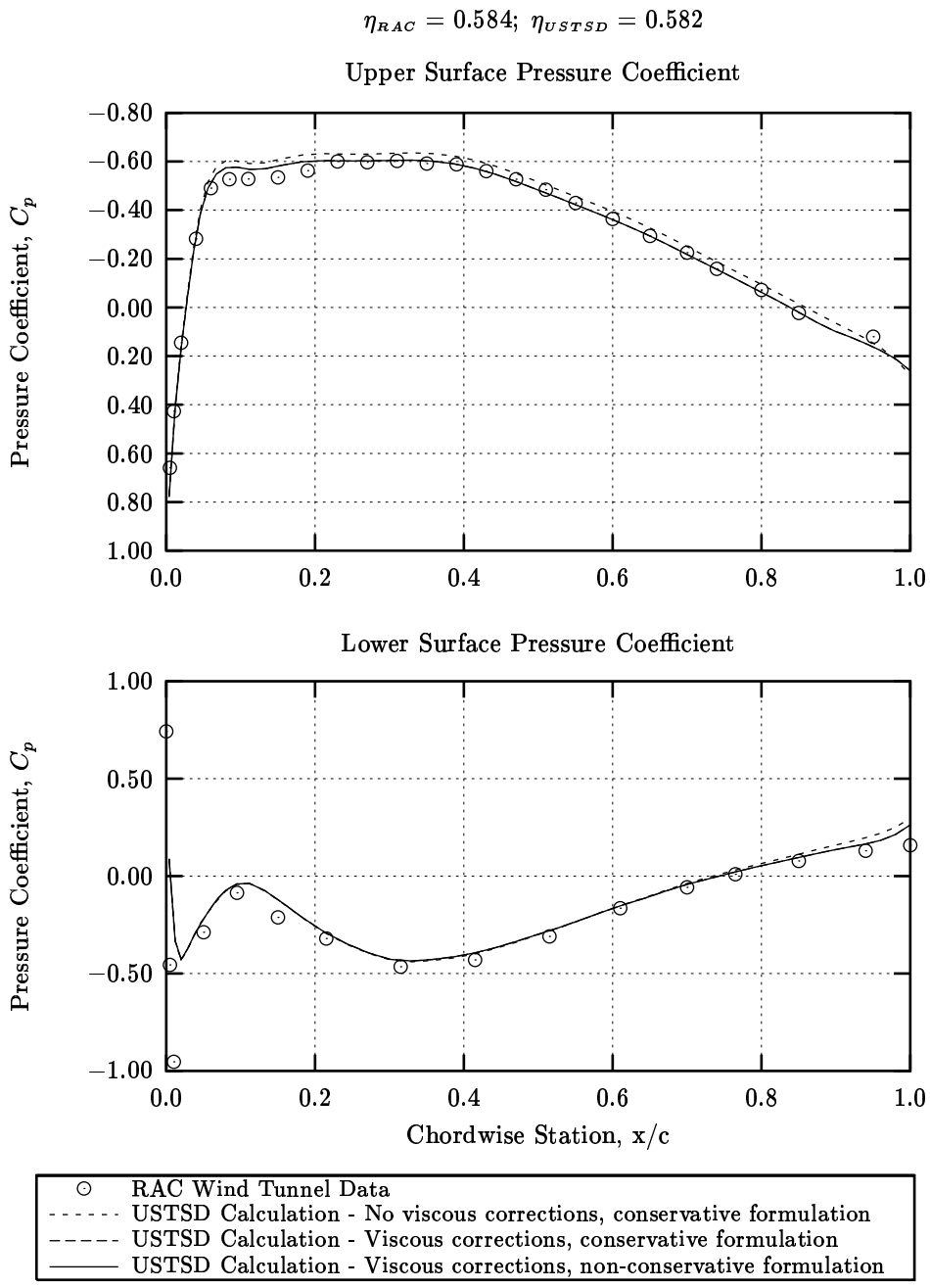

Figure 5.26: Mid pressure coefficient at 0.70 Mach number, 0.0 degrees angle of attack, 3,000,000 Reynold's number.

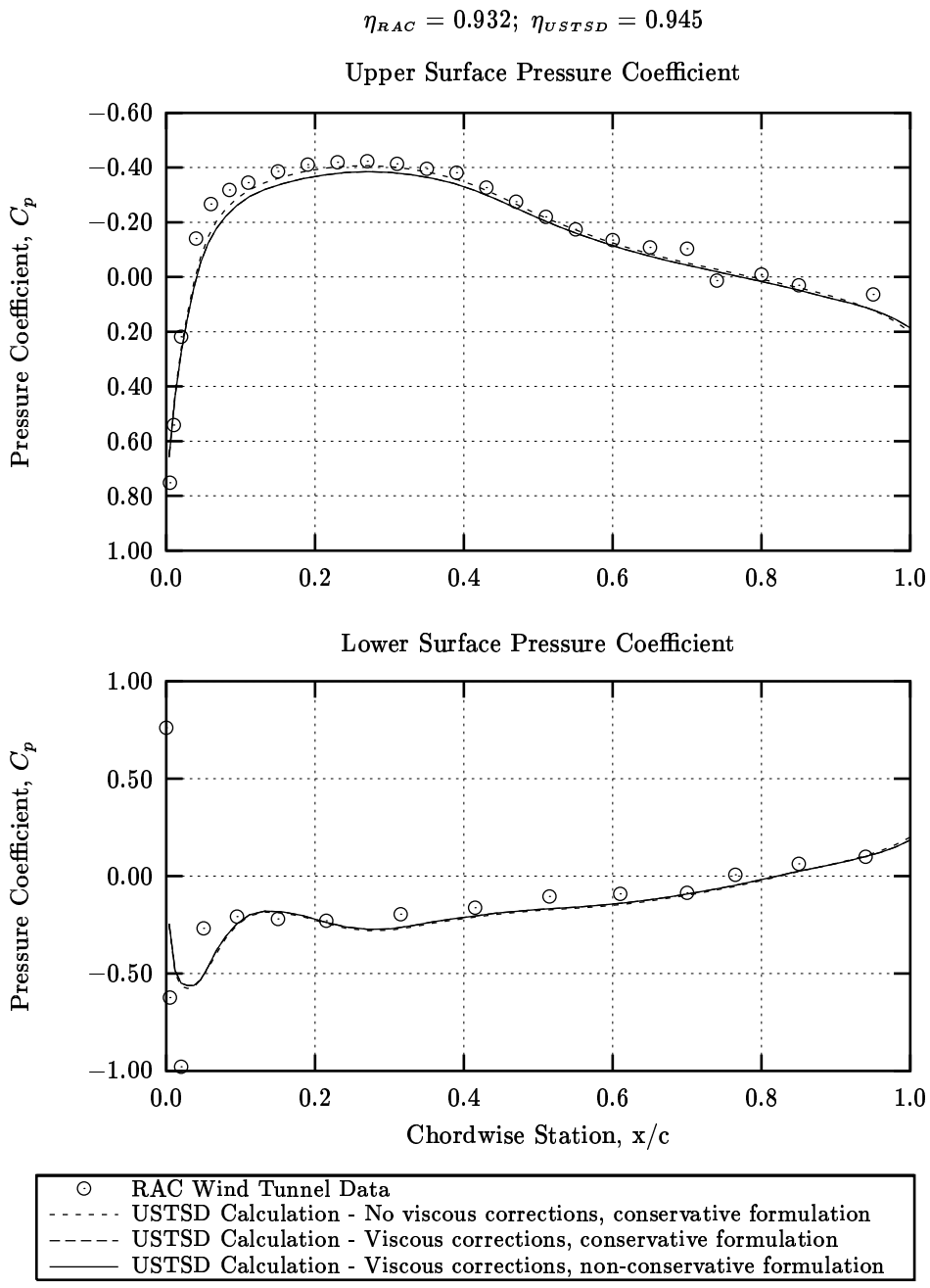

Figure 5.27: Tip pressure coefficient at 0.70 Mach number, 0.0 degrees angle of attack, 3,000,000 Reynold's number.

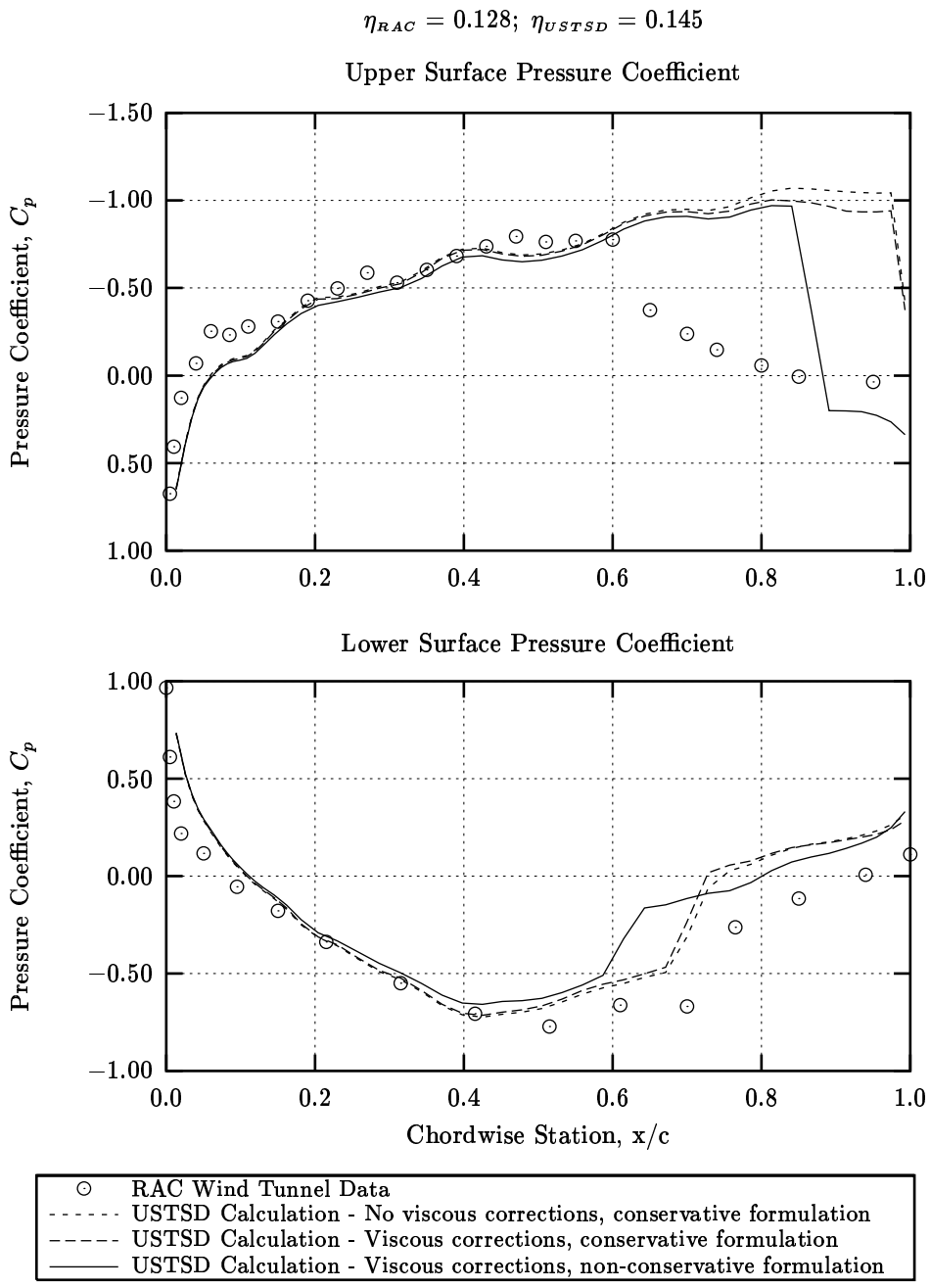

Figure 5.28: Root pressure coefficient at 0.85 Mach number, 0.0 degrees angle of attack, 3,000,000 Reynold's number.

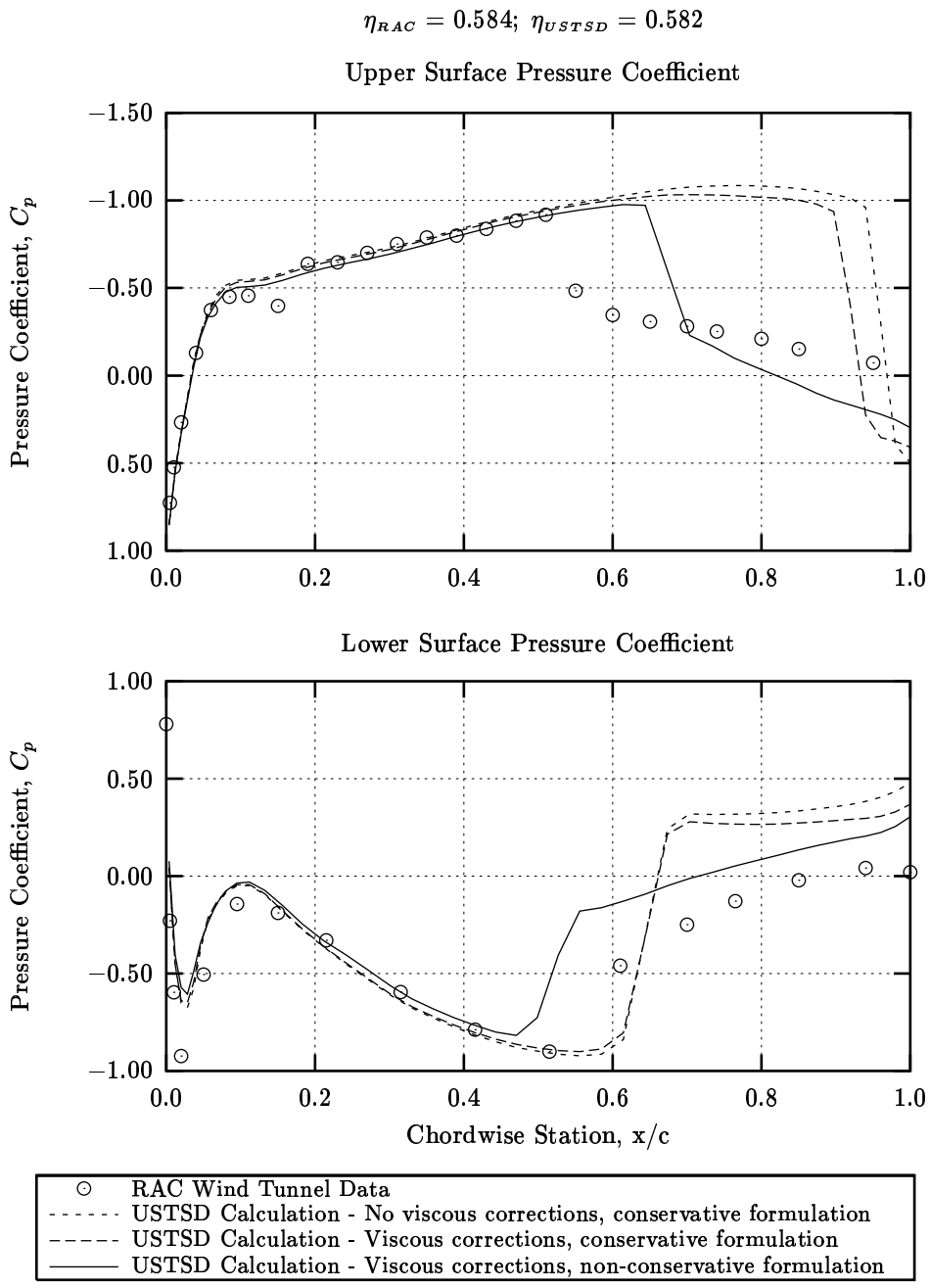

Figure 5.29: Mid pressure coefficient at 0.85 Mach number, 0.0 degrees angle of attack, 3,000,000 Reynold's number.

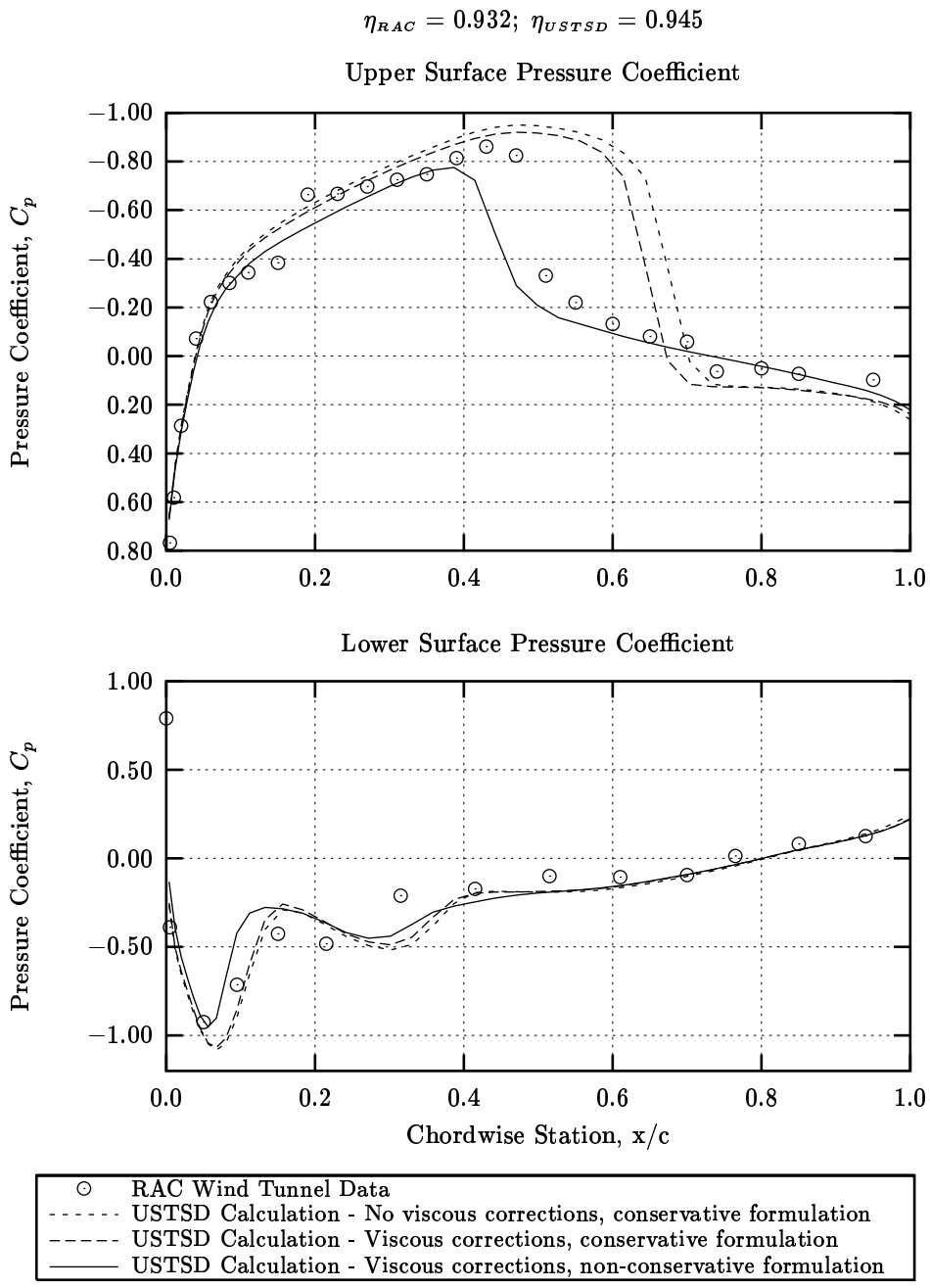

Figure 5.30: Tip pressure coefficient at 0.85 Mach number, 0.0 degrees angle of attack, 3,000,000 Reynold's number.

Chapter 6

Aeroelastic Results & Analysis

The results of the aeroelastic analysis of the Hawker 800XP are presented in this chapter. No experimental data is available with which to compare the results. The trends of the solutions are compared with the trends in Reference [5] and the difference in results between the conservative and non-conservative solutions are discussed.

6.1 Flutter Curve

The unsteady aerodynamic calculations were performed at Mach numbers 0.60, 0.70, 0.80, 0.85 and 0.90. Solutions were obtained for Mach numbers 0.60, 0.70 and 0.80. Above Mach 0.80, the variation in artificial damping was such that no flutter point could be resolved. The flutter results are summarized in Table 6.1 and Table 6.2.

The conservative and non-conservative flutter curve for the Mach 0.60 solution is presented in Figure 6.1. Both solutions were obtained at a density of 3.00E-4 ($slug/ft^3$), which corresponds to a U.S. Standard Atmosphere altitude of 54,000 feet. At Mach 0.60, the conservative and non-conservative solutions exhibit the same trend in variation of artificial damping, except at the low end of the flutter speed. A higher flutter speed is calculated from the non-conservative solution than from the conservative solution as a result of the difference in the predicted shock position of each solution. The discrepancy in shock position between the two formulations is discussed in Section 5.5. The flutter speed from the conservative calculation is 788.1 (ft/s) at a frequency of 16.70 (Hz). The non-conservative calculation results in a

Table 6.1: Conservative flutter results.

Mach No. ($\sim$)	Density ($slug/ft^3$)	Flutter Speed (ft/s)	Dynamic Pressure ($slug/ft^3$)	Flutter Frequency (Hz)
0.6	3.00E-04	788.1	93.2	16.70
0.7	2.20E-04	910.8	91.1	16.33
0.8	1.50E-04	1015.7	77.5	14.98

Table 6.2: Non-Conservative flutter results.

Mach No. ($\sim$)	Density ($slug/ft^3$)	Flutter Speed (ft/s)	Dynamic Pressure ($slug/ft^3$)	Flutter Frequency (Hz)
0.6	3.00E-04	798.9	95.7	16.73
0.7	2.20E-04	972.8	104.1	16.55
0.8	1.50E-04	1038.6	80.9	15.05

flutter speed of 798.9 (ft/s) at a frequency of 16.73 (Hz).

The conservative and non-conservative flutter curves for the Mach 0.70 solution are presented in Figure 6.2. Both solutions were obtained at a density of 2.20E-4 ($slug/ft^3$) which corresponds to an U.S. Standard Atmosphere altitude of 60,000 feet. The trend of the conservative flutter curve at Mach 0.70 does not correspond to the trend of the non-conservative flutter curve. The flutter speed calculated from the non-conservative flutter solution is greater than the speed calculated from the conservative flutter solution. The conservative flutter speed is 910.8 (ft/s) at a frequency of 16.33 (Hz). The non-conservative flutter speed is 972.8 (ft/s) at a frequency of 16.55 (Hz).

The conservative and non-conservative flutter curves for the Mach 0.80 solution are presented in Figure 6.3. Both solutions were obtained at a density of 1.50E-4 ($slug/ft^3$) which corresponds to an U.S. Standard Atmosphere altitude of 68,000 feet. The trend of the conservative flutter curve at Mach 0.80 does not correspond to the trend of the non-conservative flutter curve. The flutter speed calculated from the non-conservative solution is greater than the speed calculated from the conservative solution. The conservative flutter speed is 1016.5 (ft/s) at a frequency of 14.98 (Hz). The non-conservative flutter speed is 1038.6 (ft/s) at a frequency of 15.05 (Hz).

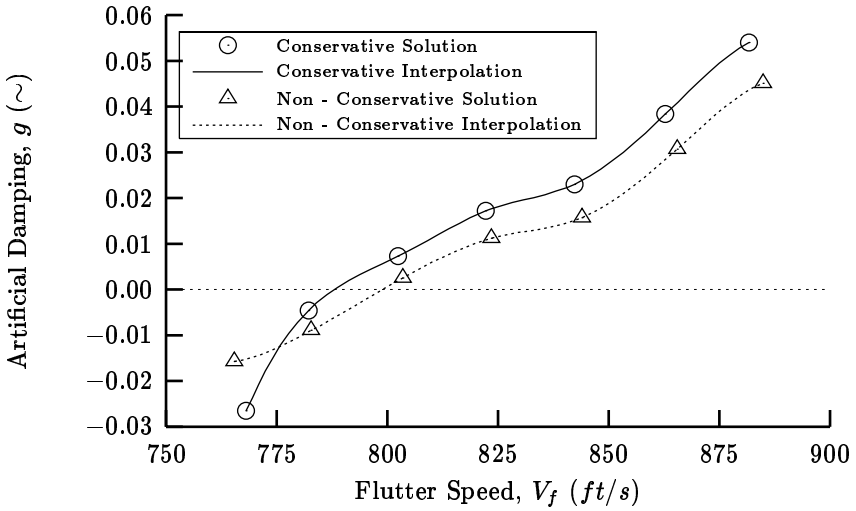

Figure 6.1: Mach 0.60 flutter curve. (Density: 3.00E-4 $slug/ft^3$)

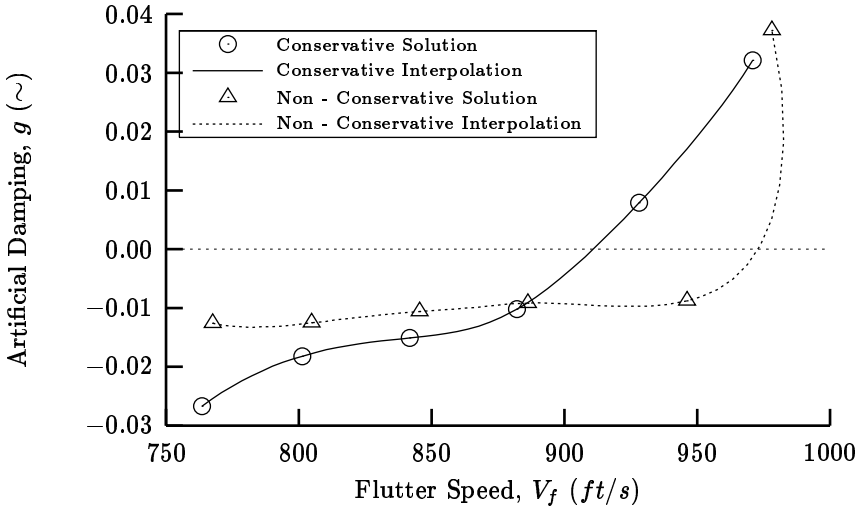

Figure 6.2: Mach 0.70 Flutter curve. (Density: 2.20E-4 $slug/ft^3$)

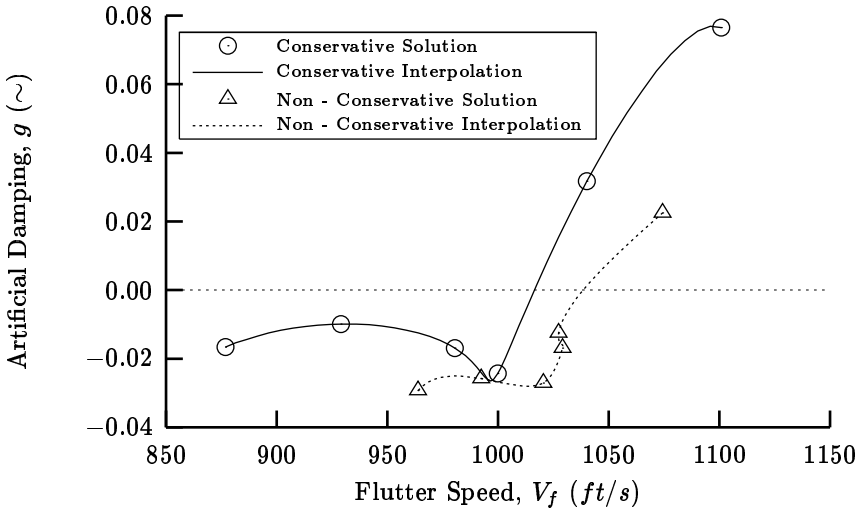

Figure 6.3: Mach 0.80 Flutter curve. (Density: 1.50E-4 $slug/ft^3$)

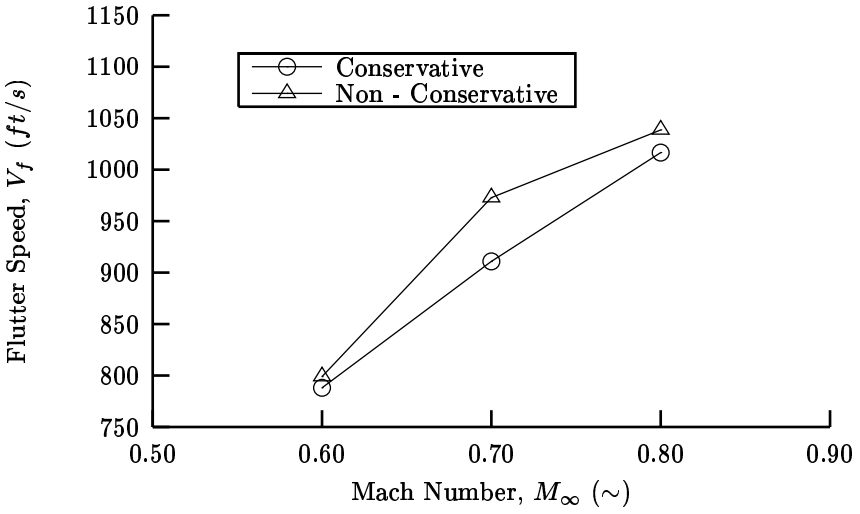

Figure 6.4: Variation of flutter speed with Mach number.

6.2 Analysis

Non-dimensionalized parameters flutter speed index and flutter frequency ratio are used to judge the USTSD flutter results. The trend of the data is similar to trends in flutter parameters observed in Reference [5]. The trend of these parameters is to decrease in value with increasing Mach number up to Mach 1.0. Beyond Mach 1.0, the parameters increase with Mach number. A rapid decrease near Mach 1.0 is the so-called "transonic dip". The transonic dip occurs in the Mach region where strong shocks, boundary layer separation and viscous effects are significant to the solution. In this analysis, the flutter speed index is defined:

$$C_f = \frac{V_f}{b_o \omega_o \sqrt{\mu}}$$

Where V_f is the flutter speed, b_o is the reference dimension, ω_o is the reference frequency and the mass ratio, μ, is defined:

$$\mu = \frac{m}{V\rho}$$

m is the mass of the wing and ρ is the flutter density. The volume, V, is the volume of a conical frustrum with a base diameter equal to the wing root chord, tip diameter equal to the wing tip chord and height equal to the wing semispan. The frustrum volume is expressed:

$$V = \frac{\pi s \left(c_t^2 + c_t c_r + c_r^2\right)}{12}$$

The reduced frequency in the USTSD program is defined:

$$k = \frac{b_o \omega_o}{V_f}$$

In this analysis, $b_o = 7.263 ft$ and $\omega_o = 17.38 Hz$. The non-dimensionalized flutter parameters are listed in Table 6.3 and Table 6.4. The flutter parameters are plotted in Figure 6.5 and Figure 6.6.

The flutter frequency ratio exhibits the expected trend of decreasing with increasing Mach number. The difference in the flutter frequency ratio between the conservative and non-conservative solution is negligible. The conservative flutter speed index also exhibits a decrease in value with increasing

Table 6.3: Conservative flutter parameters.

Mach No.	Reduced Frequency	Frequency Ratio	Mass Ratio	Flutter Speed Index
0.6	0.9673	0.961	173.5	0.0471
0.7	0.8182	0.940	236.6	0.0467
0.8	0.6726	0.862	347.0	0.0430

Table 6.4: Non-Conservative flutter parameters.

Mach No.	Reduced Frequency	Frequency Ratio	Mass Ratio	Flutter Speed Index
0.6	0.9555	0.963	173.5	0.0478
0.7	0.7766	0.952	236.6	0.0498
0.8	0.6615	0.866	347.0	0.0439

Mach number. The non-conservative flutter speed index increases at first and then decreases, nearly equal to the conservative solution. Solutions were not obtained at high enough Mach numbers to observe the transonic dip.

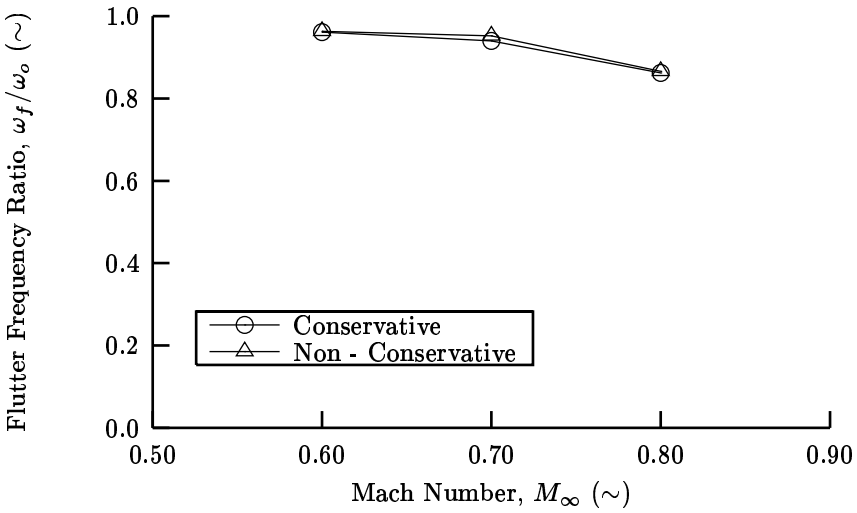

Figure 6.5: Variation of flutter frequency ratio with Mach number.

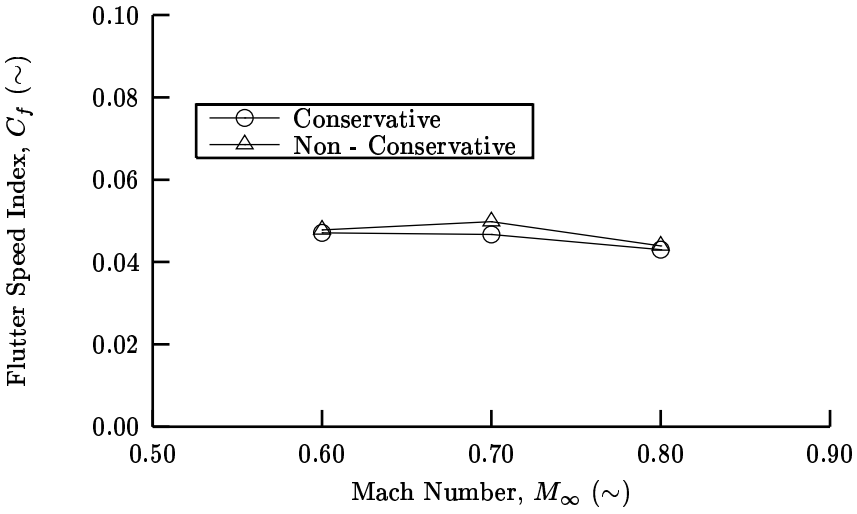

Figure 6.6: Variation of flutter speed index with Mach number.

Table 6.5: Conservative flutter eigenvector magnitude.

Ratio	Mach 0.60	Mach 0.70	Mach 0.80
q_1/q_1	1.00	1.00	1.00
q_2/q_1	3.1843	2.4468	1.2673
q_3/q_1	0.4746	0.4324	0.3245
q_4/q_1	0.0402	0.0211	0.0118
q_5/q_1	0.0254	0.0260	0.0200
q_6/q_1	0.0074	0.0091	0.0274

Table 6.6: Non-Conservative flutter eigenvector magnitude.

Ratio	Mach 0.60	Mach 0.70	Mach 0.80
q_1/q_1	1.00	1.00	1.00
q_2/q_1	3.1583	2.4897	1.2813
q_3/q_1	0.4676	0.4187	0.3351
q_4/q_1	0.0419	0.0353	0.0115
q_5/q_1	0.0241	0.0235	0.0197
q_6/q_1	0.0066	0.0068	0.0233

The relative participation of each mode in the flutter is quantified by the magnitude of eigenvectors. The normalized magnitude of the eigenvectors from the flutter solution are listed in Table 6.5 and Table 6.6. The second bending mode is the primary participant in flutter at each Mach number. The flutter frequency decreases with Mach number, evident in the increased participation of the first bending mode with increasing Mach number.

The solutions obtained indicate that USTSD provides a flutter analysis capability when there is not a strong shock jump in the flow. Flutter results were obtained below Mach 0.80. This mirrors the steady results corresponding to experimental data until Mach 0.80. Above Mach 0.80, the presence of a strong shock reduced the correspondence of the calculated shock position to the experimental shock position. In the unsteady calculation, the generalized aerodynamic forcing function would be inaccurately calculated as a result of the error in calculated shock position. Therefore, the flutter speed could not be resolved above Mach 0.80.

Chapter 7

Conclusions & Recommendations

An evaluation of the aeroelastic analysis capabilities of the USTSD code was performed. The analysis was applied to the Hawker 800XP business jet wing-fuselage configuration. A steady analysis was performed with USTSD to calculate the lift, drag, pitch and pressure coefficient. The steady results were compared with experimental data. An unsteady calculations was performed to generate the generalized aerodynamic forcing function of the flutter equation. The flutter equation was in turn solved to calculate the flutter speed. No experimental flutter data was available for comparison.

The steady results corresponded well with experiment for Mach numbers 0.70, 0.75 and 0.80. Above Mach 0.80, the position of a strong shock was not correctly calculated with USTSD, resulting in poor correlation between the calculated and experimental pressure coefficients. This was reflected in the poor correlation of the lift, drag and pitch coefficients with data above Mach 0.80. The USTSD code provided a steady transonic analysis capability when there was not a strong shock in the flow.

The unsteady analysis yielded a flutter solution for Mach numbers 0.60, 0.70 and 0.80. As with the steady results, the breakdown of the solution above Mach 0.80 could be attributed to the incorrect calculation of the shock position. Below Mach 0.80, the flutter solution trend matched flutter solution trends observed for a similar business jet configuration. In the absence of strong shocks, the USTSD code provided an aeroelastic analysis capability of business jet configurations.

To improve the capability of the USTSD to perform aerodynamic analy-

sis with the presence of a strong shock, corrections for shock-boundary layer interactions should be added to USTSD. These corrections have provided improved correlation with experiment when applied to time-domain solutions. Further improvements could be obtained by modelling the nacelle as a flow-through nacelle that is adequately covered by the grid to effect the wing. The applicability of the USTSD code aeroelastic analysis should be characterized by parameters such as Mach number, dynamic pressure, mass ratio, reduced frequency, angle of attack and airfoil thickness. An analysis of the sensitivity of the results to the structural dynamics data should also be performed.

Bibliography

[1] John T. Batina. Unsteady Transonic Small-Disturbance Theory Including Entropy and Vorticity Effects. *Journal of Aircraft*, 26(6), June 1989.

[2] Robert M. Bennett and John W. Edwards. An Overview of Recent Developments in Computational Aeroelasticity. In *29th AIAA Fluid Dynamics Conference*, number AIAA 98-2421, June 15-18 1998.

[3] Earl H. Dowell, editor. *A Modern Course in Aeroelasticity.* Kluwer Academic Publishers, Boston, third edition, 1995.

[4] John W. Edwards. Transonic Shock Oscillations and Wing Flutter Calculated With an Interactive Boundary Layer Coupling Method. *NASA Technical Memorandum*, (TM-110284), August 1996.

[5] Michael D. Gibbons. Aeroelastic Calculations Using CFD for a Typical Business Jet Model. *NASA Contractor Report*, (CR-4753), 1996.

[6] Paulo Greco, C. Edward Lan, and Tae Lim. Unsteady Transonic Aerodynamics in Frequency Domain and Calculation of Flutter Characteristics of Aircraft. In *General, Corporate and Regional Aviation Meeting and Exposition*, number 951182. SAE, May 3-5 1995.

[7] Paulo Celso Greco, Jr. *Transonic Flutter and Limit Cycle Oscillations.* PhD thesis, University of Kansas, March 1996.

[8] C. Hsu. Calculation of Unsteady Pressure Distributions and Dynamic Stability Parameters by an Unsteady Transonic Small-Disturbance Theory in the Frequency Domain. Master's thesis, University of Kansas, 1994.

[9] H. Hwang. *Computation of Unsteady Transonic Flow About Airfoils in the Frequency Domain Using the Full-Potential Equation.* PhD thesis, University of Kansas, 1988.

[10] J. A. Krupp. The Numerical Calculation of Plane Steady Transonic Flows Past Thin Lifting Airfoils. *Boeng Scientific Research Laboratories*, (D180 12958-1), June 1971.

[11] KU Flight Research Lab. Development of an Unsteady Transonic Small-Disturbance Aerodynamic Code for Flutter Prediction. Technical Report KU-FRL-1039-9, University of Kansas, May 1996.

[12] C. Edward Lan. User's Manual for an Unsteady Transonic Small-Disturbance Aerodynamic Code for Flutter Prediciton. Technical Report KU-FRL-1039-5, KU Flight Research Lab, April 1996.

[13] H. Lomax, F. R. Bailey, and W. F. Ballhaus. On the numerical simulation of three-dimensional transonic flow with application to the C-141 wing. *NASA Technical Note*, (TN-D-6933), 1973.

[14] A. H. Nayfeh and D.T. Mook. *Nonlinear Oscillations.* John Wiley Sons Publication, 1979.

[15] Perry A. Newman and Jerry C. South, Jr. Influence on Nonconservative Differencing on Transonic Streamline Shapes. *AIAA Journal*, 14(8), 1976.

[16] David Nixon, editor. *Unsteady Transonic Aerodynamics*, volume 120. Progress in Astronautics and Aeronautics, 1989.

[17] T. H. Sun. *Unsteady Transonic Aerodynamics in Frequency Domain for Flutter Analysis.* PhD thesis, university of Kansas, 1991.